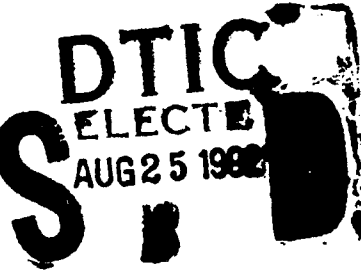


AD-A254 265

REPORT DOCUMENTATION PAGE

Form Approved
OMB No. 0704-0188

Public reporting burden for this collection of information is estimated to average 1 hour per response, including the time for reviewing instructions, searching existing data sources, gathering and maintaining the data needed, and completing and reviewing the collection of information. Send comments regarding this burden estimate or any other aspect of this collection of information, including suggestions for reducing this burden, to Washington Headquarters Services, Directorate for Information Operations and Reports, 1215 Jefferson Davis Highway, Suite 1204, Arlington, VA 22202-4302, and to the Office of Management and Budget, Paperwork Reduction Project (0704-0188), Washington, DC 20503.

1. AGENCY USE ONLY (Leave blank)	2. REPORT DATE	3. REPORT TYPE AND DATES COVERED
	1992	THESIS
4. TITLE AND SUBTITLE		5. FUNDING NUMBERS
A Model to Estimate the Flux of Back-ground Particles Expected To Accumulate On The Collector Foils of The Interstellar Gas Experiment On The Long Duration Exposure Facility Spacecraft		
6. AUTHOR(S)		
Paul A. Gehred, Captain		
7. PERFORMING ORGANIZATION NAME(S) AND ADDRESS(ES)		8. PERFORMING ORGANIZATION REPORT NUMBER
AFIT Student Attending: Utah State University		AFIT/CI/CIA-92-069
9. SPONSORING / MONITORING AGENCY NAME(S) AND ADDRESS(ES)		10. SPONSORING / MONITORING AGENCY REPORT NUMBER
AFIT/CI Wright-Patterson AFB OH 45433-6583		
11. SUPPLEMENTARY NOTES		
12a. DISTRIBUTION / AVAILABILITY STATEMENT		12b. DISTRIBUTION CODE
Approved for Public Release IAW 190-1 Distributed Unlimited ERNEST A. HAYGOOD, Captain, USAF Executive Officer		
13. ABSTRACT (Maximum 200 words)		
  92-23501 92 8 24 010		
14. SUBJECT TERMS		15. NUMBER OF PAGES
		77
		16. PRICE CODE
17. SECURITY CLASSIFICATION OF REPORT	18. SECURITY CLASSIFICATION OF THIS PAGE	19. SECURITY CLASSIFICATION OF ABSTRACT
		20. LIMITATION OF ABSTRACT

A MODEL TO ESTIMATE THE FLUX OF BACKGROUND PARTICLES
EXPECTED TO ACCUMULATE ON THE COLLECTOR FOILS
OF THE INTERSTELLAR GAS EXPERIMENT ON THE
LONG DURATION EXPOSURE FACILITY SPACECRAFT

by

Paul Anthony Gehred

A thesis submitted in partial fulfillment
of the requirements for the degree

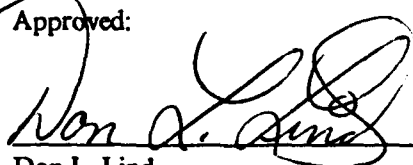
of

MASTER OF SCIENCE

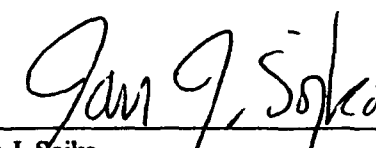
in

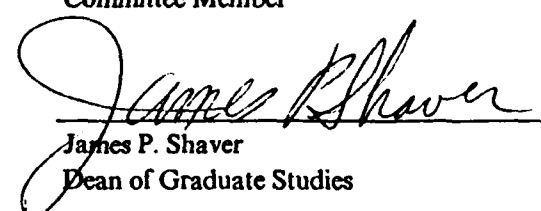
Physics
(Upper Atmospheric Option)

Approved:


Don L. Lind
Major Professor


Wolfgang Schmickler
Committee Member


Jan J. Sojka
Committee Member


James P. Shaver
Dean of Graduate Studies

UTAH STATE UNIVERSITY
Logan, Utah

1992

ACKNOWLEDGEMENTS

This research was funded by the Air Force Institute of Technology and by Utah State University. I thank the people in the Air Force who have granted me this excellent opportunity. I thank Dr. Don L. Lind for the project and his guidance. My committee members, Dr. Wolfgang Schmickler and Dr. Jan Sojka, provided timely help. I also thank Dr. John Raitt and Barbara Phillips for the physics computer lab. The physics office and the CASS office have been more than generous sharing their wares.

This paper has been aided immeasurably by the talents of Donald C. Thompson. He's the author of the plotting program used for the majority of the interesting graphs and figures which follow. Also my mentor, Dr. Bela Fejer, whose efforts have worked to turn U.S.U. into "The Cornell of the Rockies."

I also thank the members of the physics grad student office. My cubicle contained UNIX guru Raghuram Tumkur, and LDEF pro Teresa Burns. Nearby cubicles are home to fine physics rookies like Rob Davies and "the Doctors," Engelmann and Barghouti. The champion *Physica* soccer team and other students all help in little ways which go unnoticed at the time.

The rest of my thanks goes to my family. Patti, my friend, has kept the household running on all cylinders. She's been forgiving when I'm called away. Daughters Alison and Katy joyfully helped me drop my worries at the door.

DTIC QUALITY INSPECTED 2

Paul A. Gehred

Accession For	
NTIS GRA&I <input checked="" type="checkbox"/>	
DTIC TAB <input type="checkbox"/>	
Unannounced <input type="checkbox"/>	
Justification _____	
By _____	
Distribution/ _____	
Availability Codes _____	
Dist	Avail and/or Special
A-1	

TABLE OF CONTENTS

	Page
ACKNOWLEDGEMENTS	ii
LIST OF TABLES.....	v
LIST OF FIGURES.....	vi
ABSTRACT.....	ix
CHAPTER	
1. INTRODUCTION.....	1
1.1 The Interstellar Gas Experiment	1
1.2 Objectives of the Research	4
2. THE LOW EARTH ORBIT ENVIRONMENT	6
2.1 The Thermosphere	6
2.2 The MSIS Thermospheric Model	16
2.3 The Physics and Math of the MSIS Model	18
2.4 The Geometry of the Experiment	22
3. CALCULATIONS	34
3.1 Generating Input for the MSIS Model	34
3.2 An Early Estimate	38
3.3 Application of the Kinetic Theory of Gases.....	38
3.4 A Spherical Coordinates Estimation	41
3.5 The Probability of a Particle Adhering to the Foil	43
3.6 The Calculation in Cartesian Coordinates	45
3.6.1 The Limits of Integration	45
3.6.2 Calculating a Density Gradient Across Each Foil	49
3.6.3 The Integration Limits Including the Yaw of 8°	50
3.6.4 The Numerical Solution	52
3.7 The Error Function Solution	58
4. RESULTS	62
4.1 Variance of the Results.....	62
4.1.1 Varying the MSIS Input	62
4.1.2 Varying the Integration Input	64
4.1.3 Varying the Eta Function	67

4.2 Summary	71
4.3 Suggestions for Future Work	74
REFERENCES	76

LIST OF TABLES

Table		Page
2.1	Keplerian Orbital Elements of LDEF	15
2.2	Collector Viewing Angles	29
3.1	IGE Trapping Probability, The Eta Function	44

LIST OF FIGURES

Figure		Page
1.1.	A simplified sketch of the IGE experiment on the LDEF spacecraft. Each square segment represents a tray on which all experiments were attached, below is an expanded diagram of a tray.	2
2.1.	Mean monthly values of the F10.7 cm flux for the entire 70-month flight of LDEF.	7
2.2.	Mean monthly Ap geomagnetic index for the entire 70-month flight of LDEF.	9
2.3.	Variations of total atmospheric density, helium density, temperature, latitude, longitude, and local solar time during one complete orbit. Orbit inclination is equal to LDEF's, at 28.4 degrees.	10
2.4.	Annual variation in the mean monthly temperature and helium density during active solar conditions (1989).	12
2.5.	Annual variation in mean monthly temperature and helium density during quiet solar conditions (1986).	13
2.6.	The decrease in LDEF orbital altitude and the increase in velocity with time.	14
2.7.	Atmospheric temperature as a function of altitude for solar quiet and active conditions.	21
2.8.	The density of thermospheric constituents versus altitude for solar maximum at local noon.	23
2.9.	The density of thermospheric constituents versus altitude for solar maximum at local midnight.	24
2.10.	The density of thermospheric constituents versus altitude for solar minimum at local noon.	25
2.11.	The density of thermospheric constituents versus altitude for solar minimum at local midnight.	26
2.12.	The orientation of LDEF in orbit. North pole is visible, as well as six of the collectors of IGE.	27
2.13.	The orientation of the fields of view of the seven IGE collectors relative to LDEF. Positive angles are to the north of the LDEF ground track. The +110° viewing direction was capable of collecting only atmospheric helium.	28

2.14.	The location of trays H6 and H9 on the spaceward side of LDEF.	30
2.15.	The location of the collectors on the LDEF spacecraft. Above, the position of tray F6 on the south face. Below, the position of tray E12 on the north face.	31
2.16.	The dimensions of tray H6 located on the spaceward side of LDEF, above, and the dimensions of tray F6 on the south face, below.	32
2.17.	The dimensions of each collector housing.	33
3.1.	Average local AM values of temperature and helium density at LDEF altitude for the duration of the flight.	36
3.2.	The average PM values of temperature and helium density at LDEF altitude for the duration of the flight.	37
3.3.	A summary of key facts of the LDEF orbit.	39
3.4.	A summary of typical thermospheric parameters at orbit altitudes, averaged over the entire 69-month flight of LDEF.	40
3.5.	The trapping probability eta, as a function of velocity. The boxed data points are experimental results, the diamond points are calculated estimates.	46
3.6.	Lines representing the field of view for the midpoint of the foil on collectors oriented normal to the direction of motion.	47
3.7.	Lines representing the field of view of all collectors oriented normal to the direction of motion in v_y , v_z space, neglecting the yaw of 8°	48
3.8.	Lines representing the field of view for collector three on tray H6.	49
3.9.	A profile of a foil collector housing. The foil cassette is visible at the base. The dashed lines represent the field of view for foil region 1, the downwind side of the foil, and for foil region 5, the upwind side.	51
3.10.	The helium particle density on the foil after LDEF's flight. First data point is on the downwind side of the foil, last data point is on the upwind side of the foil.	54
3.11.	A three-dimensional plot of the helium density gradient across the foils, neglecting the 8° yaw.	55
3.12.	A three-dimensional representation of the helium density found on foil cassette 4 including the yaw. This applies to foils oriented perpendicular to the orbital velocity.	56

3.13.	A three-dimensional display of helium density with position on foil cassette 5. This distribution includes the eight degree yaw and the effect of the tray baffle on the upwind side of tray H9.	57
3.14.	A comparison of results for the number of helium particles per square meter of foil. The solid line represents the triple integral solution, the dashed line represents the error function solution.	60
4.1.	The variance of MSIS computed temperature and helium density with universal time.	63
4.2.	The variance of MSIS computed temperature and helium density with the longitude of right ascension at the ascending node, RAAN.	65
4.3.	A comparison of integration results for December, 1988, for foil cassette 3. The local solar time was segmented into eight three-hour bins, and two 12-hour bins, each with a mean temperature and density.	66
4.4.	Maxwellian velocity distributions for helium with zero bulk flow velocity and density of $3(10)^{12} \text{ m}^{-3}$. The top plot had temperature of 1400 °K, the bottom plot temperature was 700 °K.	68
4.5.	A plot of an overestimate or high eta (solid line), and an underestimate, low eta, (dashed line) of the probability of a particle adhering to the foil.	69
4.6.	The results for cassette 1 using the error function method. The dashed lines represent limits of uncertainty due to the eta function.	70
4.7.	The results for cassette 2 using the error function method. The dashed lines represent limits of uncertainty due to the eta function.	72
4.8.	The results for cassette 3 using the error function method. The dashed lines represent limits of uncertainty due to the eta function.	73
4.9.	A comparison of parameters of interstellar helium and atmospheric helium.	74

ABSTRACT

**A Model to Estimate the Flux of Background Particles
Expected to Accumulate on the Collector Foils
of the Interstellar Gas Experiment on the
Long Duration Exposure Facility Spacecraft**

by

Paul A. Gehred, Master of Physics

Utah State University, 1992

**Major Professor: Dr. Don L. Lind
Department: Physics**

The Interstellar Gas Experiment (IGE) on board the Long Duration Exposure Facility (LDEF) exposed metallic foils to the interstellar wind to collect noble gas particles from outside of the solar system. The terrestrial helium present in the atmosphere at low Earth orbit altitudes was also collected on the foils, along with the interstellar helium particles.

In order to discriminate between the desired interstellar helium and the background terrestrial helium particles, an analysis of the expected distribution of atmospheric helium on the foils was conducted. This analysis used the principles of the kinetic theory of gases to simulate the state of the thermosphere for the entire 69-month flight of LDEF. The key parameters needed to apply the kinetic theory of gases were the temperature and density of the helium at LDEF altitude. This information was calculated using the Mass Spectrometer and Incoherent Scatter (MSIS) model.

The entire duration of the flight was split into 70 month-long intervals. For each of these intervals, mean values for the kinetic temperature and helium density were calculated. These values were calculated twice per month, once for the AM period and once for the PM period, in local solar

time. The average altitude and orbital speed were also calculated for each month. The integration program was fed 140 sets of values of these parameters.

The density gradient of the accumulated particles was calculated using the Maxwellian velocity distribution together with the limiting geometry of the foil collector housing. The collector housing walls defined the field of view of each foil. The field of view changed slightly with the position on the foil. For each month, the integration calculated the flux at five different positions across the center of each foil. The limits of the field of view were used as the limits of integration in three-dimensional velocity space.

Another variable in the integration was the probability that a particle which struck the foil would actually adhere to it. This probability was a function of the velocity of the particle. An experiment conducted in 1983 provided a set of 18 data points. These data points were fitted to a curve called the eta function, which provided continuous probability values for any chosen velocity. Some ambiguity in the data for this function suggested solving the integration with an underestimation and with an overestimation of the eta function in order to give a range of uncertainty for the possible solutions.

Results of the calculations depend on the orientation of the collector with respect to the orbital velocity. For the midpoint of foils which were tilted perpendicular to the orbital motion, the expected helium accumulation was $5(10)^6$ helium atoms per square meter of foil. For collector three, which was dipped 24° into the direction of orbital motion, the expected accumulation was $5(10)^8$ atoms per square meter. Collector two was dipped 24° out of the direction of orbital motion, and was expected to accumulate only $6(10)^5$ atoms per square meter. Due to the uncertainty in the eta function these values are plus or minus at least an order of magnitude.

The mass spectrometer analysis conducted so far has found traces of ^3He , ^4He , ^{20}Ne , and ^{22}Ne . Since MSIS only provided data for the ^4He , estimated values of the other isotopes were based on the relative abundances proportional to ^4He . The result of this research will hopefully supply the experimenters with values to be subtracted out of the final concentration. The remainder will provide information on the density of the interstellar wind and the isotope ratios of the noble gases.

interstellar wind. This information will aid research of nucleosynthesis and provide new clues regarding the origin of the universe.

(88 pages)

CHAPTER 1

INTRODUCTION

1.1 The Interstellar Gas Experiment

The purpose of the Interstellar Gas Experiment (IGE) was to collect and isotopically analyze the noble gas component of the interstellar medium. The scientific significance of the data to be derived from the direct detection of interstellar particles is in understanding nucleosynthesis. Current techniques for determining relative abundances of stellar elements rely on stellar spectroscopy. This technique falters when applied to noble gases because the interpretation depends strongly on assumptions about the atmospheric structure of the source [Lind *et al.*, 1988]. The isotopic ratios can also be determined more readily with the mass spectrometer analysis.

The collection device used in the IGE was made up of seven metallic foils. High energy noble gas particles impacting the foils became lodged in the metal lattice. These seven collectors were placed on the Long Duration Exposure Facility (LDEF) with different fields of view. These view angles optimized the chance for the authors of the experiment to recognize the angular distribution of the interstellar gas particles. The solar gravitation field focuses the interstellar wind into a type of stream. As the LDEF spacecraft revolved into the leeside of the sun, it bathed in this stream with its collectors opened perpendicular to the flow.

Each collector contained six beryllium-copper foils which acted as film. The foils were stacked on top of each other in a unit called a foil cassette. Each foil could be flipped out of the way, exposing the next foil of the cassette. The experiment was designed to expose each foil for a period of several weeks. Then a timer would trigger the end of exposure for the previous foil and expose a new foil. This enabled a temporal and spatial analysis of the distribution of particles in the interstellar gas. If everything had gone as planned, the foils would be retrieved after one year in space, by a subsequent shuttle mission. However, the Challenger tragedy delayed the shuttle mission schedule. As a result, the LDEF spacecraft orbited for almost six years. Figure 1.1 shows a simplified outline of the LDEF spacecraft, with locations of the IGE collectors sketched in.

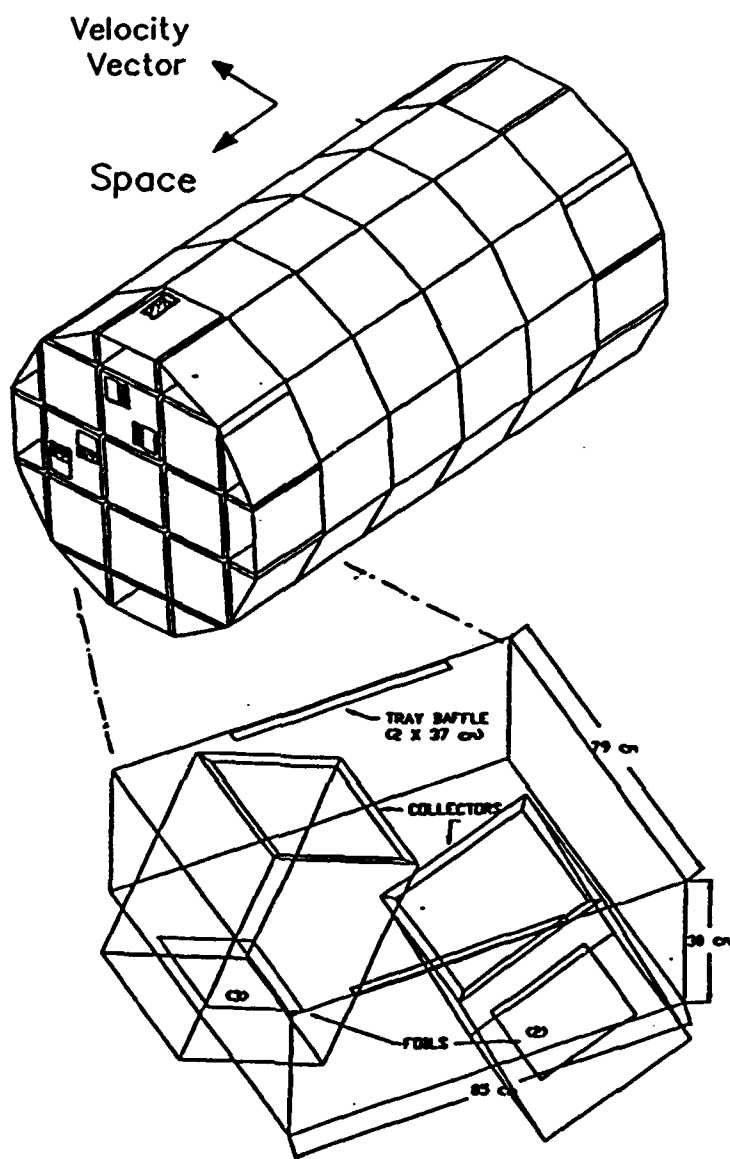


Fig. 1.1. A simplified sketch of the IGE experiment on the LDEF spacecraft. Each square segment represents a tray on which all experiments were attached, below is an expanded diagram of a tray.

After recovery of LDEF, a new surprise was discovered. The initiate relay for the exposure timer had stuck. Because this relay failed, the foils never cycled through their scheduled exposure times. Each collector exposed only one foil for the entire flight. The experiment designers recalculated a computer simulation with this new information. Some of the temporal and spatial information was lost by the relay failure but the ability to identify interstellar gas particles was not.

Discriminating between atmospheric noble gas constituents and interstellar noble gases is crucial to the experiment. The foils were placed at the bottom of each collector housing. The housing acted to filter out ambient helium particles because they were serrated and baffled to prevent easy access to the foils. Five of the collectors were oriented perpendicular to the direction of motion. Nevertheless, a certain amount of terrestrial helium was expected to imbed into the foils. To better estimate this unwanted flux of helium, one collector, number seven, was oriented towards the Earth solely to measure background particles. The Earth would prevent any interstellar particles from accessing number seven's foils. Two collectors, numbers two and three, were tilted along the direction of motion. The orientation of all seven collectors will be discussed in chapter 3 below.

The foils are currently undergoing mass spectrometer analysis at the University of Bern, Switzerland. Special techniques are required for measuring the minute quantities of interstellar gas. At first relatively low temperatures (450°C) are used to release the least tightly bound particles. These low energy particles will contain the greatest proportion of background contamination, helium from the atmosphere. At higher temperature steps, particles which penetrated deeper into the foils will progressively be released. This analysis will provide information on how much kinetic energy the interstellar gas particles possessed.

Early results from Switzerland indicate helium and neon have been found on the foils. The expected particle concentration pattern has been suggested by the early analysis. Intensity gradients across each foil have also been found. This analysis could provide important data on the synthesis of light nuclei in the early universe and the beginning processes of nucleosynthesis and galactic evolution [Lind *et al.*, 1991].

1.2 Objectives of the Research

The goal of this research was to numerically estimate the number of atmospheric noble gas particles expected to accumulate on each foil. Since each foil had a concentration gradient due to the shadowing effect of the collector housing, this gradient was also calculated. With the flux of ^4He particles calculated, ^3He concentration was estimated using known ratios.

The state of the thermosphere must be determined to calculate the flux of atmospheric helium impinging on the foils. In particular, the temperature and density of helium at low Earth orbit (LEO) altitudes must be given in order to apply kinetic theory. Since no measured data specific to the LDEF orbit exists for these parameters, a model was adopted, the Mass Spectrometer and Incoherent Scatter model (MSIS) created by A.E. Hedin and his associates at Goddard Space Flight Center. MSIS is the international reference atmosphere for the thermosphere. It provides temperature and density values for the main neutral constituents of the atmosphere.

The problem was broken into two parts. The first part involved providing the MSIS model all the necessary inputs it required. To receive the temperature and density data, the model requires information for specific location, altitude, local solar time, and universal time. The MSIS input parameters also require the F10.7 cm flux, and the geomagnetic Ap indicator. The F10.7 cm flux is an indicator of total solar energy output. The Ap indicator is an average value which provides information on the geomagnetic field. Both of these indicators track the changes in solar output as the solar cycle progresses. The F10.7 cm fluxes and Ap values were accessed from the National Center for Atmospheric Research archives. Solving the orbit equation at a specific time provided the exact location, local solar condition, and altitude of LDEF. The calculated values of helium density and temperature were stored for the integration process.

The integration, the second part of the problem, used the principles of kinetic theory. The atmosphere was assumed to be in thermal equilibrium, with large numbers of particles interacting through elastic collisions. This allowed the Maxwell-Boltzmann velocity distribution function to represent the state of the thermosphere, at low Earth orbit altitudes. This distribution function is

defined so that $f(r, v, t)$ is the number of molecules at position $r + dr$, with velocity between v and $v + dv$, at time t . The thermal equilibrium assumption allows the use of the Maxwell-Boltzmann velocity distribution function:

$$F(v_x, v_y, v_z) = f(v_x)/f(v_y)f(v_z) = (m/2\pi kT)^{3/2} \exp(-mv^2/2kT) \quad (1.2.1)$$

Where m is the mass of the particle, T is the temperature, k is Boltzmann's constant, and:

$$v = (v_x^2 + v_y^2 + v_z^2)^{1/2}$$

v is the velocity of the particle. By integrating the Maxwell-Boltzmann velocity distribution function over all possible velocities, every particle is represented or accounted for.

$$\int \int \int_R F(v_x, v_y, v_z) dv_x dv_y dv_z = 1$$

At this point, MSIS gives the number of helium particles per unit volume and the distribution function gives the probability of finding that particle with a specific velocity. This is all that is required to determine what fraction of the helium molecules are able to hit the foil. An experimentally determined function was included to find the probability that a particle hitting the foil would actually adhere in the lattice. Various differences in look angle were modelled by changing the limits of integration. This permitted the calculation of the concentration gradient across each foil. The limits of integration were modified to represent the seven different fields of view and the differences in the geometry between collectors.

Since this is a probabilistic analysis special care must be taken to account for sources of error. Uncertainties will arise due to assumptions in the derivation of the Maxwell-Boltzmann equation, the MSIS model results, and in the function for the probability of the particle imbedding in the foil based on its momentum. The error analysis will be detailed in chapter 4.

CHAPTER 2

THE LOW EARTH ORBIT ENVIRONMENT

The LDEF spacecraft orbited the Earth for almost six years in the portion of the atmosphere known as the thermosphere. This region responds to changes in solar activity. The discussion below will examine how solar activity changes the density, temperature, and composition of the thermosphere. Then it will examine the MSIS model and finally, turn to the geometry of the experiment.

2.1 The Thermosphere

The Interstellar Gas Experiment was launched into low Earth orbit (LEO) in the bay of space shuttle Challenger, in April, 1984. On April 7, the crew deployed LDEF into a stable orbit at 475 km altitude. When LDEF was retrieved in 1990, its altitude had decreased to 320 km. NASA captured it perhaps a month before it would have re-entered in a free fall meltdown; therefore, this description of the thermosphere will focus on the LDEF orbit. In particular, it will concentrate on the 300 to 500 km altitude range, at low latitudes, during the time April, 1984 to January, 1990.

Neutral gases outnumber the charged particles by six orders of magnitude at these heights. This tenuous atmosphere is in thermal equilibrium. Temperatures and densities respond to the daily effects of the sun, but slowly, with 24 hour cycles. Likewise, there are enough collisions to keep temperature and density spatially continuous and slowly changing. Thermospheric winds rarely exceed one percent of the virtual wind produced by the spacecraft hurtling through a calm atmosphere.

In the spring of 1984, when LDEF was launched, the sun's magnetic activity was declining as the solar cycle waned. From 1985 through the end of 1987 key indicators of solar output remained consistently low. This is called a "quiet sun," or solar minimum period. The F10.7 cm wavelength is

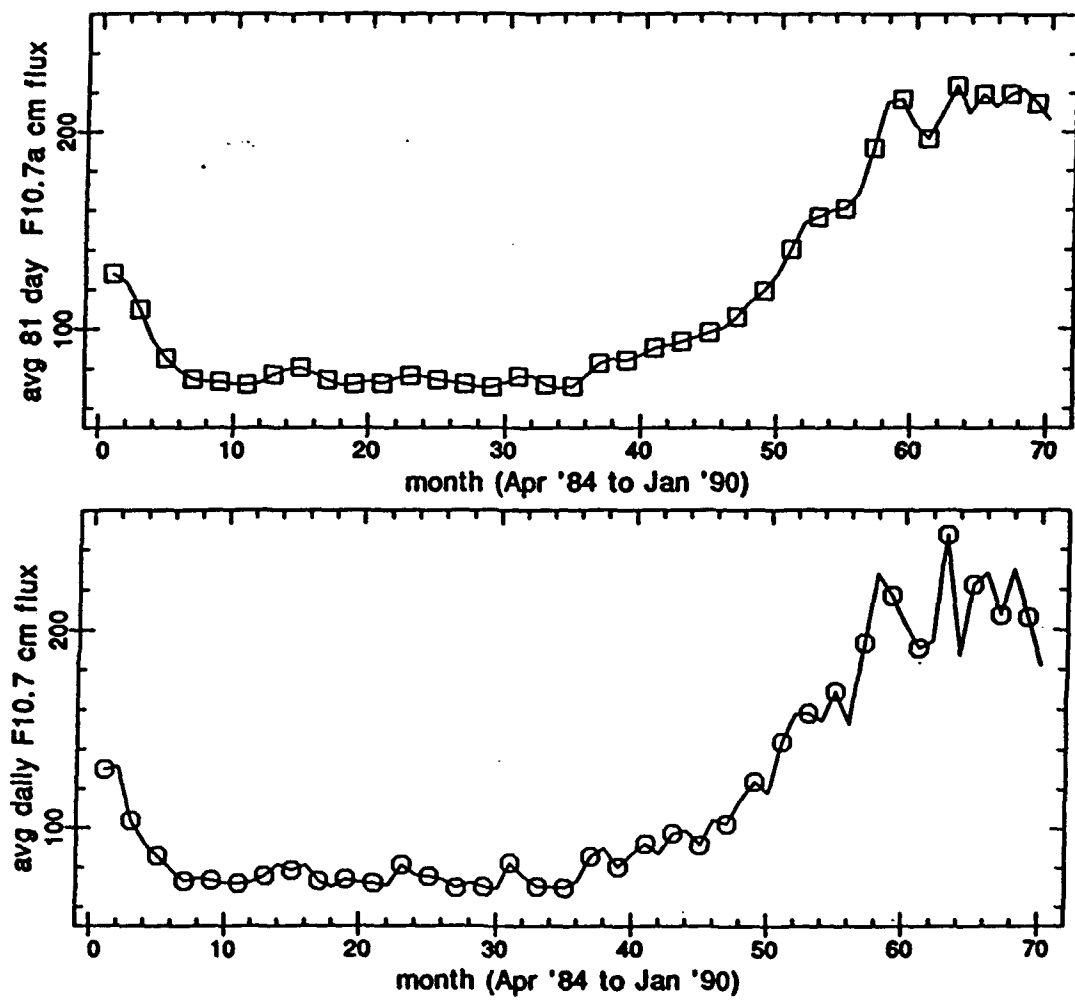


Fig. 2.1 Mean monthly values of the F10.7 cm flux for the entire 70-month flight of LDEF.

accepted by aeronomers as an indicator of total solar extreme ultraviolet flux (EUV). MSIS uses a daily F10.7 cm value and an 81 day average value as inputs. Figure 2.1 presents these two indicators, averaged over the entire month, for the duration of the spacecraft's flight. The figure shows the rising solar flux beginning in month 45, January, 1988.

The Earth's magnetic field responds to changes in solar output also. The geomagnetic field creates large atmospheric disturbances during magnetic storms, particularly at high latitudes. MSIS models the neutral components. The charged particles energize the neutrals during these storms. The geomagnetic indicator needed for the model is the Ap index, a global average of magnetogram variances. The Ap index begins as the Kp index, a logarithmic value taken every three hours at 12 stations around the globe. It is then converted to the ap index, which is a linear value. The Ap index is the result of a daily average of the three hour ap values [Knecht and Shuman, 1985]. Figure 2.2 graphs the monthly average of the Ap values during LDEF's flight. The peak Ap average value of 43 occurred in stormy March, 1989.

Since the ambient LEO atmosphere is sensitive to solar cycle changes, it's clear that daily sunrise and sunset will produce profound changes in the state of the gas. At sunrise, the temperature at altitude has reached its nadir. As solar energy heats the gas through EUV absorption, the temperature rises about 50 °C per hour, peaking just prior to sunset. This heating produces a corresponding expansion of the gas at local solar afternoon. This diurnal bulge of high pressure remains at the subsolar point. Observers on the Earth measure a diurnal tide "pulled" by the sun. Figure 2.3 illustrates these diurnal variations for one full orbit. An interesting effect can be seen in this figure. The total atmospheric density peaks in late afternoon as the temperature peaks, but helium density often peaks toward sunrise.

The plotted orbit has an inclination of 28 degrees with an altitude of 400 kilometers. The relevant solar indices supplied to MSIS for August 1989 were an Ap of 20 and F10.7 cm daily flux of 223. The 81 day average F10.7 cm flux was 219. These high values represent the onset of solar cycle 22 which would peak in 1991. From January 1989 on, LDEF orbited in a thermosphere agitated by an "active" sun. Typical F10.7 cm fluxes were near 200, and Ap indices were near 20 for the

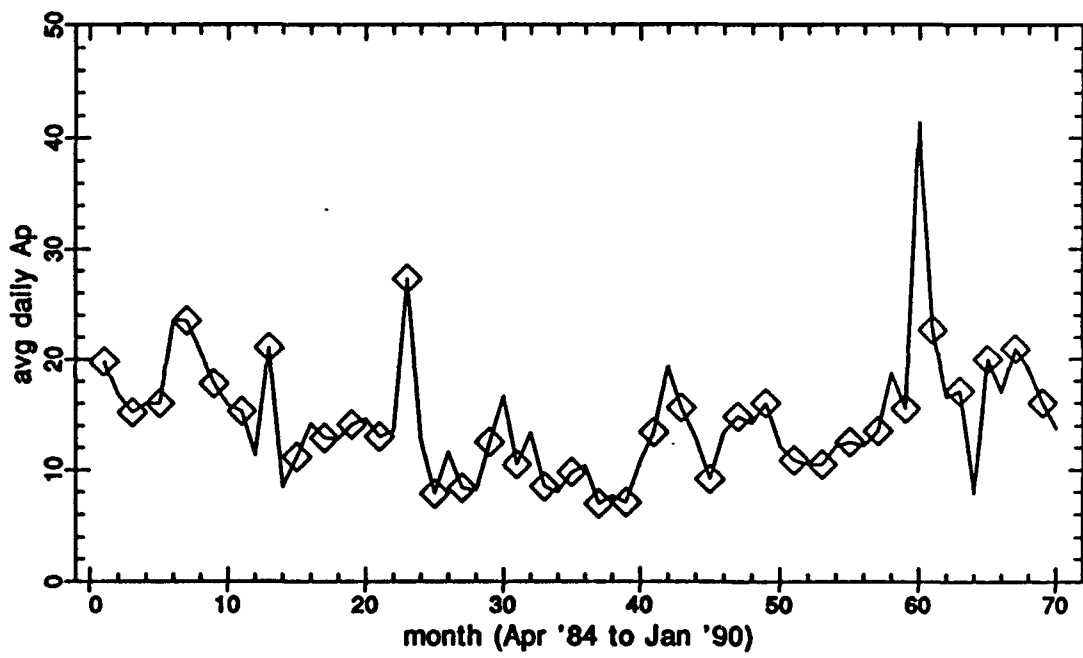


Fig. 2.2 Mean monthly Ap geomagnetic index for the entire 70-month flight of LDEF.

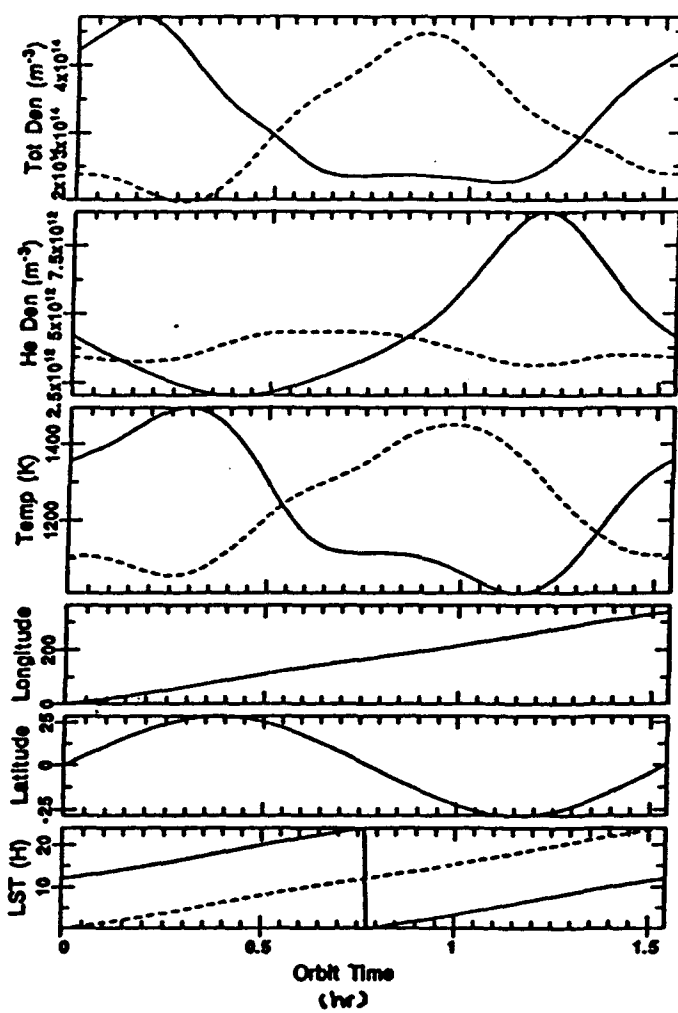


Fig. 2.3. Variations of total atmospheric density, helium density, temperature, latitude, longitude, and local solar time during one complete orbit. Orbit inclination is equal to LDEF's, at 28.4 degrees.

remainder of the LDEF's journey.

These two effects, the daily rise and fall in temperature associated with the Earth's rotation, and the long term influence of steadily increasing solar activity, cause the largest change in the state of the atmosphere at LEO altitudes. Another modulated change occurs because of the Earth's revolution about the sun. There is a bulge of higher densities at constant altitude due to the equinoxes. Figure 2.4 illustrates this effect for 1989. Figure 2.5 illustrates the same effect during solar quiet time in 1986. A comparison of values between 1986 and 1989 shows that the active sun produces a thermosphere which is warmer by 400 °C and richer in helium density by a factor of two.

Another important effect became significant in 1989 also. The denser atmosphere introduced larger drag and LDEF began its descent in earnest. Figure 2.6 graphs the decrease in altitude for the 70-month flight. Placed in orbit at 475 km, altitude decreased to 320 km by January, 1990. The slope of the curve indicates how little time NASA had left to recapture LDEF. As the spacecraft fell, it also accelerated. Its velocity increased from 7.6 km/sec to 7.7 km/sec.

The remaining considerations cause smaller changes to occur in the state of the thermosphere. The MSIS model requires specific inputs for location, year, date, universal time, and local solar time. Each piece of information alters the computed values for temperature and helium density. For example, if all other inputs are held constant, with the date changing by five days, MSIS returns values for temperature and density which differ because of slight changes due to the Earth's new position in its orbit about the sun. The MSIS model's response to variations in the input parameters will be examined in chapter 4.

Knowing exactly where LDEF was, at any given time, could be calculated using the Keplerian orbital elements found in table 2.1. Notice the eccentricity is approximately zero. This implies a nearly circular orbit. The orbit was assumed to be circular for this calculation.

LDEF's orbital inclination of 28 degrees kept it at low latitudes. The thermosphere behaves differently in the tropics compared with the poles. Strong geomagnetic storms have a large effect on polar wind fields. Ions, driven along magnetic field lines, produce enough drag on the neutrals to alter circulation. The influx of storm energy dissipates gradually by heating the neutrals. This

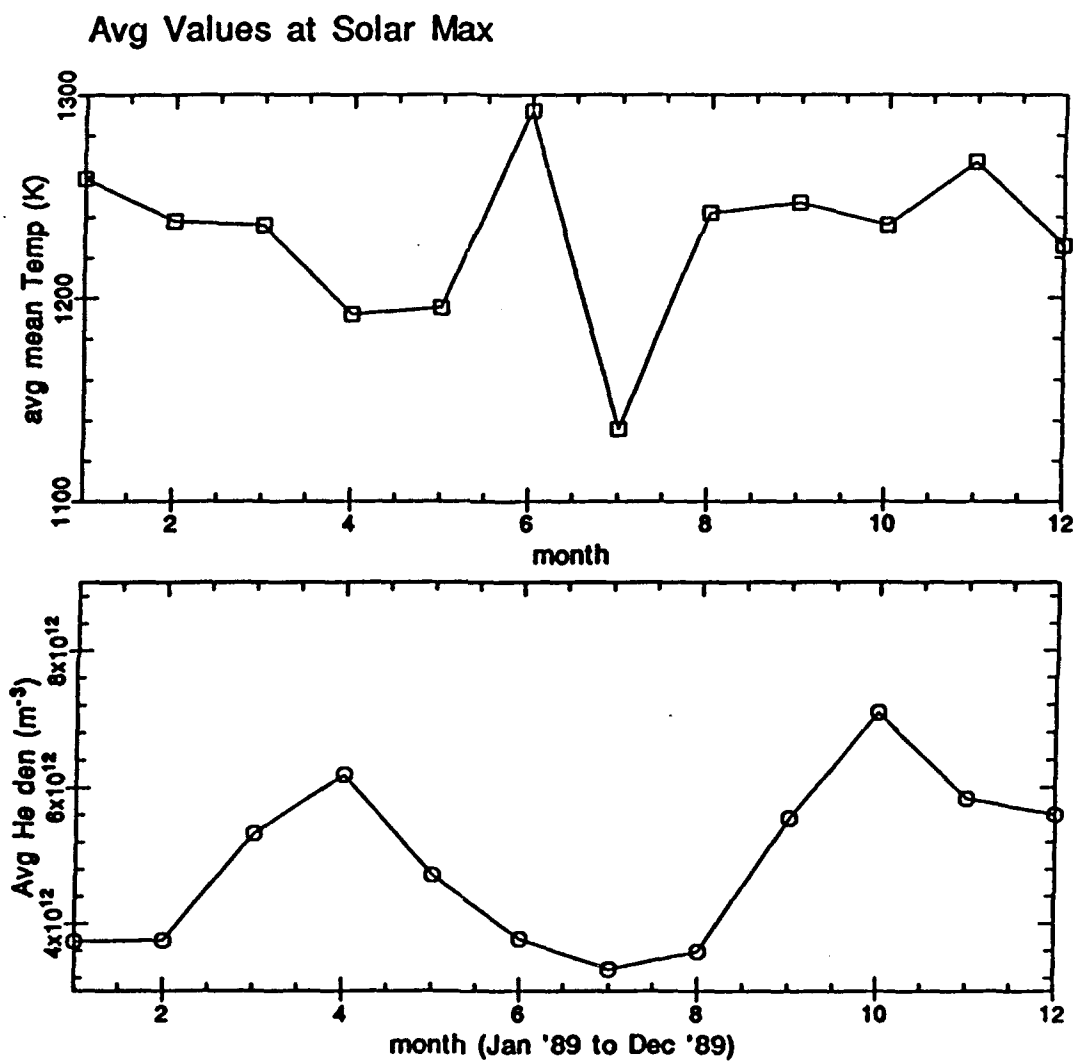


Fig. 2.4. Annual variation in the mean monthly temperature and helium density during active solar conditions (1989).

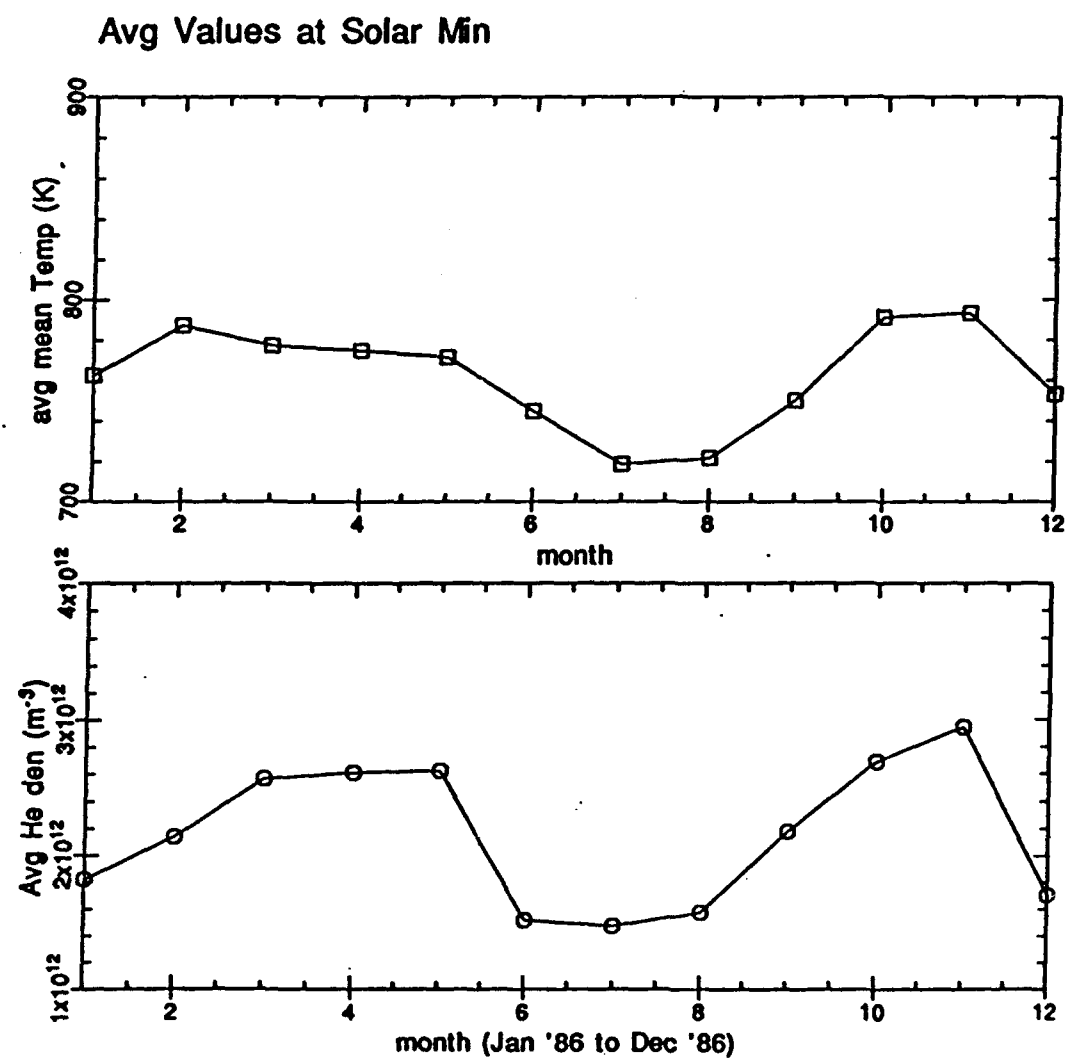


Fig. 2.5. Annual variation in mean monthly temperature and helium density during quiet solar conditions (1986).

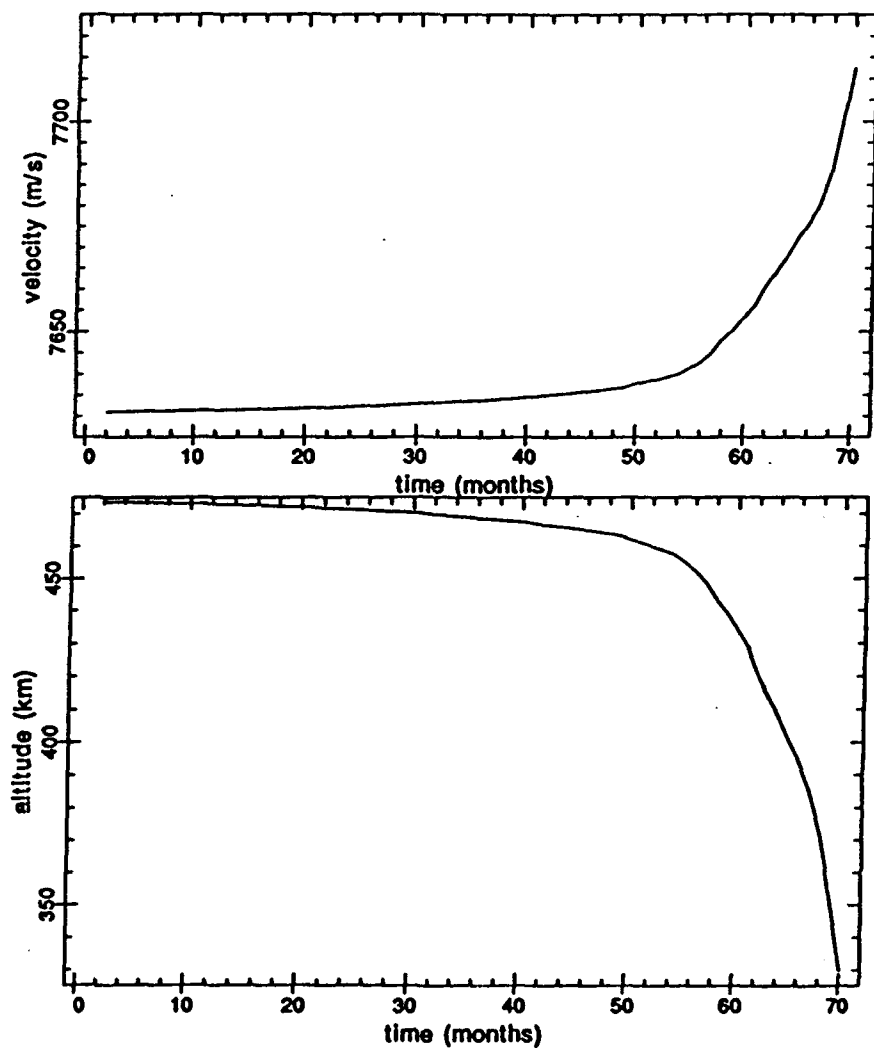


Fig. 2.6. The decrease in LDEF orbital altitude and the increase in velocity with time.

Table 2.1 Keplerian Orbital Elements of LDEF.

Orbital Element (units)	At Launch	At Docking
Semimajor Axis (km)	6861	6715
Eccentricity	0.00141	0.00152
Inclination (degrees)	28.3709	28.4826
Argument of Perigee	53.2328	7.2505
Rt. Ascension Ascnd. Node	228.409	147.934
True Anomaly	345.352	0.2738
Altitude (km)	474	325
Precession Rate (deg/day)	-6.802	-7.281

produces a region of higher pressure which affects low latitude density and temperature in due time.

The complexity of this situation can hardly be overstated. Consider the following: the bulk of the corpuscular and joule heating occurs at the poles, but the subsolar, high-energy heating and direct energy injection by the ring current mechanism also produce a low latitude density disturbance. There is a response time for each effect. Typically, it takes four to six hours for polar density waves to reach low latitudes. The magnitudes of the density disturbances are also damped with time [Pfleiss, 1982].

It has also been shown that different chemical constituents respond to storms differently. Helium and atomic oxygen densities decrease in the auroral zone and increase at low latitudes. Nitrogen increases quickly in direct relation to geo-magnetic activity. Height variations also arise, and atomic oxygen is depleted at low altitudes, but increases at higher altitudes where the effect of increased temperature is more important than transport effects [Engebretson and Mauersberger, 1983; Hedin *et al.*, 1977; Hedin *et al.*, 1981].

The climatological circulation of the thermosphere behaves like a Hadley cell during quiet sun conditions. This cellular flow features a low latitude region of rising warm air, a high altitude poleward flow, sinking at the poles, and finally a low altitude southward flow. During active periods, storms produce enough heat to create a second cell pattern, the opposite of the Hadley circulation. In the tropics, average storm circulations are damped enough to show little effect on the Hadley flow. This flow is generally two orders of magnitude less than LDEF's orbital velocity [Killeen and Roble, 1988]. The low latitude effect called the equatorial electrojet is capable of generating zonal winds of over 150 m/s. This strong current occurs below 120 km altitude [Fejer, 1991]. Its effect at LDEF's altitude is not well understood. Both the electrojet and the Hadley circulation were assumed to be negligible for this project.

Thermospheric research continues to find new relationships about how incoming energy effects the density, composition, and temperature of the gas. The atmosphere responds both spatially and temporally. This complex behavior has been modelled by the MSIS programmers. Aeronomers have relied on this semi-empirical model for almost twenty years. A close look at MSIS results will help to better understand LDEF's orbital environment. The following section examines the MSIS model, including a brief look at how it works.

2.2 The MSIS Thermospheric Model

What is a "model atmosphere"? It can consist of tables, graphs, or software which show distributions of pressure, temperature, and gas concentration. Neutral models are based on experimental data and fitted to the data using least square's best fit techniques. Some neutral models in use today include the U.S. Standard Atmosphere, the Jacchia Reference Atmosphere, and the Atmospheric Handbook. Continuous fields may now be interpolated from known data points according to the principles of an ideal gas in hydrostatic equilibrium. Since the thermosphere responds to changes in solar activity and geomagnetic activity, an effective model must include the option to input the proper indicators of this activity.

The earliest models of the neutral thermosphere were based primarily on total densities inferred from satellite drag analysis done by L. G. Jacchia in the early 1960s. Incoherent scatter data showed significant differences with the results of these models [Sojka, 1989]. Hedin's MSIS model began with the analysis of *in situ* measurements from a neutral mass spectrometer aboard the Ogo-6 satellite. Ogo-6 flew from June, 1969 until July, 1971. Its perigee was at 400 km with an apogee of 1100 km. The instrument measured molecular nitrogen, atomic oxygen, and helium. Hedin's 1973 model provided a faithful representation of thousands of measured data points. As a bonus, it also revealed many global distribution features which were inherent in the data but were never as apparent as this before [Hedin *et al.*, 1974].

Hedin gathered more results from satellites and incoherent scatter radars and incorporated them into the model. The most significant of these were from the Neutral Atmospheric Composition Experiment and the Open Source Spectrometer experiment aboard the AE-C satellite. He used the incoherent scatter findings to improve the exospheric temperature fit. He added three new constituents into the model: argon, hydrogen, and molecular oxygen [Hedin *et al.*, 1977]. This influx of new measurements tightened the outputs adherence to real-time *in situ* data. McPherson and Rishbeth used Malvern data and subjected MSIS to a test in 1979. Their objective was to examine the temperature portion of the model with data obtained outside the range from which it was constructed. They found only minor discrepancies [McPherson and Rishbeth, 1979].

At this point the weakest temperature modelling agreement came at high latitudes for high magnetic activity. Another weak area was in composition measurements at altitudes below 140 km. The biggest upgrade in MSIS-86 came from including new data from the Dynamics Explorer satellite, DE-B. This provided strong coverage of the polar regions. Terms were added to better represent seasonal variations near the poles under both quiet and magnetically disturbed conditions. N, atomic nitrogen, was also added to the menu. The MSIS-86 model is the accepted COSPAR International Reference Atmosphere (CIRA) for the thermosphere [Hedin, 1987, 1991].

The most recent version, MSISE-90, includes the mesosphere and lower stratosphere. It provides aeronomers with "a single analytic model for calculating temperature and density profiles

representative of the climatological average for many geophysical conditions" [Hedin, pg. 1159, 1991]. For the helium calculations below, both the 1986 and 90 editions were used. I asked Dr. Hedin about this. He replied, "In general, MSISE-90 is virtually the same as MSIS-86 above 120 km" [personal correspondence, 1991]. Hedin concludes, "The model represents current knowledge of the climatological average reasonably well" [personal correspondence, 1991]. It certainly has increased the level of complexity since the original satellite drag models of the 1960's.

2.3 The Physics and Math of the MSIS Model

Hedin's group faced the task of reproducing the temperature and composition profile of the neutral thermosphere for any location, at any time, under any solar and geomagnetic condition. Armed with the laws of classical mechanics, and assuming an ideal gas in hydrostatic equilibrium, the Goddard team proceeded to develop the model's code.

They knew the largest variations from climatological mean values were caused by solar activity. The sunspot record has been documented since the 1700s. The periodic fluctuations of the solar cycle also occur in the extreme ultraviolet (EUV) wavelengths. EUV radiation absorbed in the thermosphere creates the bulk of the heating which drives neutral temperatures from 200 K to well over 1000 K every day. A review glance at figure 2.1 shows how the F10.7 cm flux varied across the six year orbit of LDEF. A preview glance at figure 3.1, a diagram of MSIS computed temperature and density values, shows the same trend. Clearly, the solar EUV output forces the greatest response by the thermosphere.

The spherical shape of the Earth causes differential heating with respect to latitude. The Earth's rotation and revolution create large variations in insolation with respect to local time, and time of the year. The atmosphere reacts to strong heating at the subsolar point by expanding and creating a diurnal tidal bulge. This creates a pressure forcing which drives neutral winds. The model doesn't attempt to reproduce the dynamics of the thermosphere but it must consider these winds because they cause tidal changes in the density at any location. Another global feature of the low latitude neutral atmosphere is the midnight pressure bulge formed by thermal tides. This bulge

rotates at the anti-solar meridian [Herrero and Merriweather, 1980]. Hedin sorted the data into three hour blocks to preserve the cyclic tides with harmonics of 24-, 12-, and 8-hour periods.

The complexities of modelling the climate of the thermosphere are imposing. The code development began with first principles, so Hedin and his associates began with the ideal gas law:

$$p = nkT$$

p is the pressure, n is the number density, k is Boltzmann's constant, and T is the temperature.

Another fundamental equation needed was the hydrostatic equation:

$$\frac{dp}{dh} = -nmg$$

Here h is the height, m is the particle's mass, and g is the gravitational acceleration. These equations can be combined to produce:

$$-\frac{1}{p} \frac{dp}{dh} = \frac{mg}{kT} = \frac{1}{H} \quad (2.3.1)$$

with H in meters defined as the pressure scale height. In the thermosphere, for a given constituent, both g and T will be functions of height. The foundation of all neutral density models rests on the fact that equation 2.3.1 is consistent at any level where diffusive separation exists and where the distribution is determined only by the vertical pressure gradient balancing against gravity. Below 100 km altitude, equation 2.3.1 holds if a weighted average mass is used to represent the masses of all the atmospheric constituents.

Integrating equation 2.3.1 with height gives the variation of pressure with height above any chosen base level, h' , at which pressure is p' :

$$p = p' \exp\left[\frac{(h'-h)}{H}\right] \quad (2.3.2)$$

When this expression is iterated to account for changes in gravity and temperature with height, it gives reasonable results for number densities of constituents. When number densities are

known, along with a base level temperature, equation 2.3.2 can be solved for the unknown temperature. A note of caution here: there is no guaranty that diffusive equilibrium holds. Gravity waves can induce turbulence which will often bring low level density values to higher regions. In general, the results of this model will be climatologically reasonable, not exact.

The task of keeping the results close to real values involved fitting curves to thousands of in situ data points gathered from satellites and measurements from incoherent scatter radars. The model uses an exponential temperature profile as a function of geopotential height for the upper thermosphere and an inverse polynomial in geopotential height for the lower thermosphere. These temperature profiles allow exact integration of the hydrostatic equation for a constant mass to determine the diffusive equilibrium density profile for each important species. The exospheric temperature and density of each species at 120 km are expressed as a function of local time, latitude, longitude, universal time, F10.7, and Ap using spherical harmonics for latitude versus local time or longitude variations (up to degree 4) with Fourier series in time of day (up to third harmonic) and day of year (up to 2nd harmonic), and polynomials for variations with F10.7 index and Ap index [Hedin, 1991].

The merit of an empirical model based on a spherical harmonic analysis is that these functions are mutually orthogonal. They form a complete set that can in principle represent any degree of complexity in the data by a systematic increase in the number of coefficients used. Since the spherical harmonics are approximate eigenfunctions in the thermosphere, relatively few terms are needed. Analysis in terms of these components can aid in understanding the origin of various thermospheric variations [Hedin *et al.*, 1974; Mayr and Volland, 1970].

Figure 2.7 displays MSIS data for temperature during different solar conditions. Note how little temperature varies with altitude at LEO heights. Above 300 kilometers temperature is nearly constant. This is called the exospheric temperature. This figure also shows how increased solar output, indicated by the F10.7 cm parameter, changes the gas temperature. If the F10.7 cm flux is increased from 50 to 250, the temperature at altitude goes from 680 °K to 1400 °K. Lastly, figure 2.7 shows the range in temperature caused by local solar time effects. The temperature difference

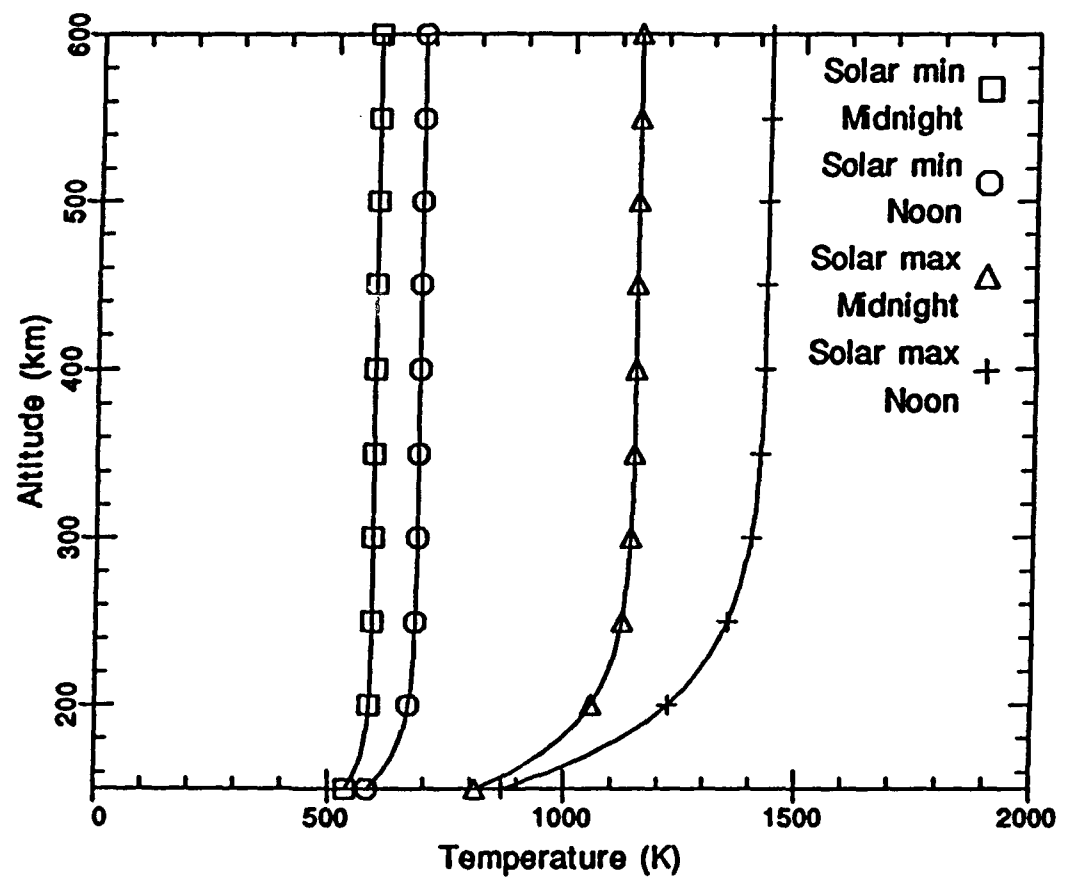


Fig. 2.7. Atmospheric temperature as a function of altitude for solar quiet and active conditions.

between local solar noon and local midnight is 30 percent during active conditions.

The next few figures show the variability of neutral components under differing solar conditions. Figure 2.8 graphs the density of atmospheric species as a function of altitude during solar maximum at local noon. Likewise, figure 2.9 shows densities during solar maximum at midnight. Figure 2.10 shows densities during solar minimum for local noon. Helium density hovers near $2(10)^{12}$ (m^{-3}) during quiet sun. The density doubles during active sun. One important feature to note is in figure 2.11, where the helium density dominates the thermosphere at LDEF altitudes above 450 km, during solar quiet, at midnight.

The MSIS model does an effective job portraying the make-up of the thermosphere. The figures show the fleeting changes the LEO atmosphere undergoes as it responds to solar forces. The next section turns to the physical limits of the Interstellar Gas Experiment.

2.4 The Geometry of the Experiment

LDEF carried seven IGE collectors. Each exposed a thin sheet of foil to a different region of the sky. This section will illustrate the regions of the sky each collector viewed. It will also describe these collectors in detail.

LDEF can crudely be described as a cylinder, with a height twice its diameter. The external surface of LDEF held numerous experiments. Each experiment was attached to a tray roughly one square meter in size. Each tray was given a designation such as H6, or E12. The tray designation indicated its position on the spacecraft.

A useful coordinate system to describe the orbit can be defined using the focus of the orbital path and the direction of motion. Figure 2.12 shows how the orbiting spacecraft was oriented. The Z axis can be defined as the line connecting the center of gravity of the Earth with the center of gravity of LDEF. The positive Z direction will be towards deep space. The positive X direction will be defined as the velocity vector. This fixes the Y coordinate as positive to the north.

When LDEF was deployed, the launch introduced no spin about the Z axis. This enabled each collector to have a fixed viewing angle along the YZ plane. LDEF was gravity gradient stabilized

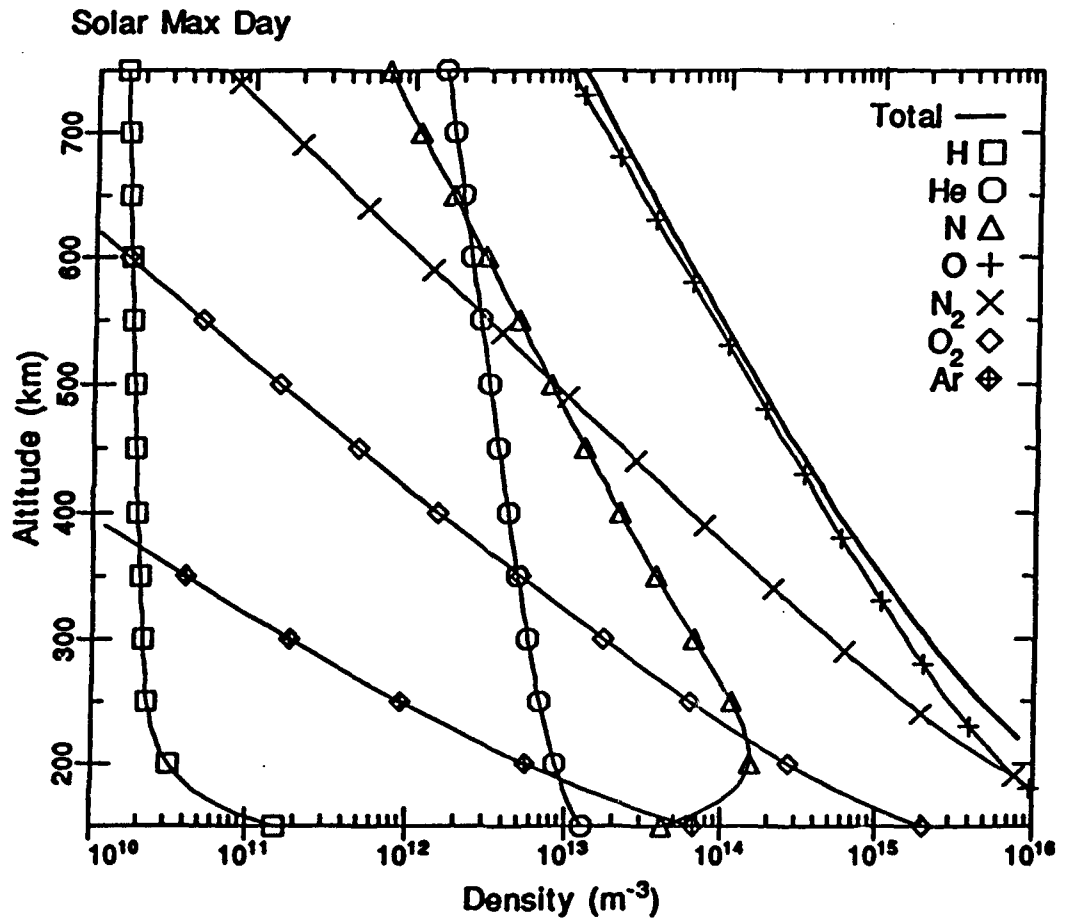


Fig. 2.8. The density of thermospheric constituents versus altitude during solar maximum at local noon.

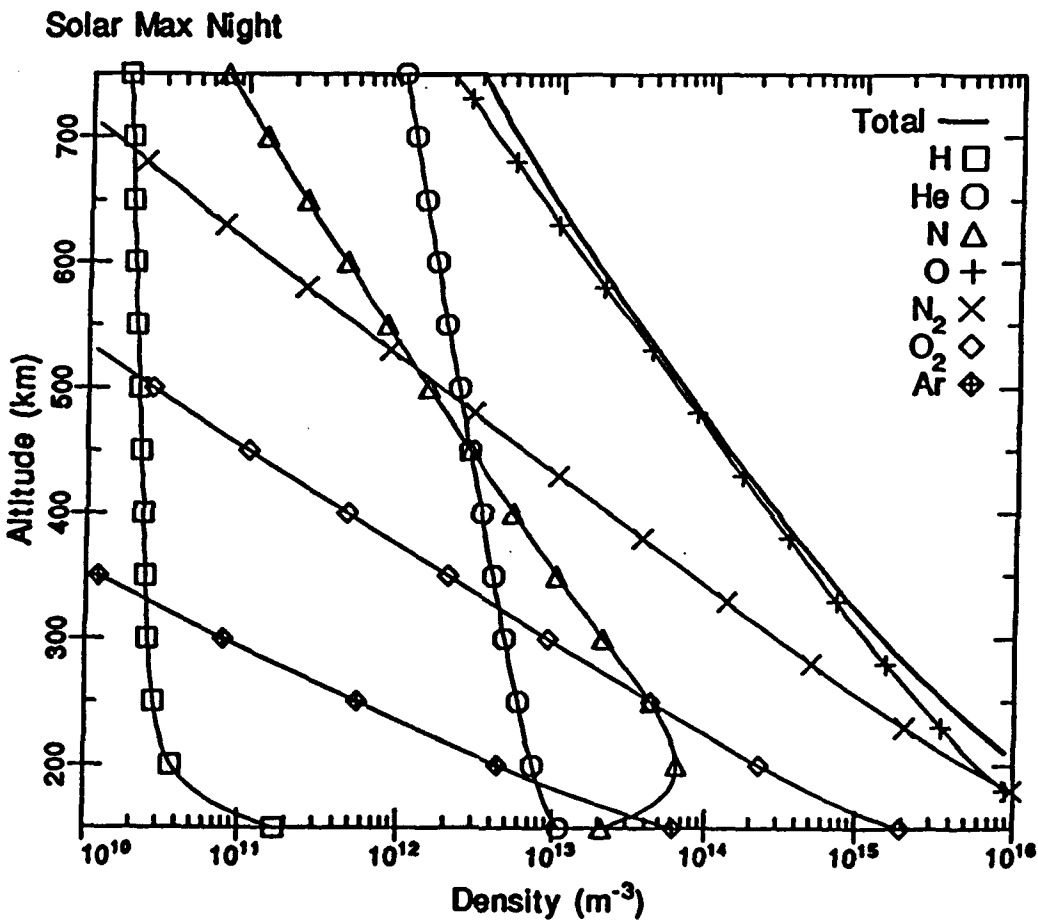


Fig. 2.9. The density of thermospheric constituents versus altitude for solar maximum at local midnight.

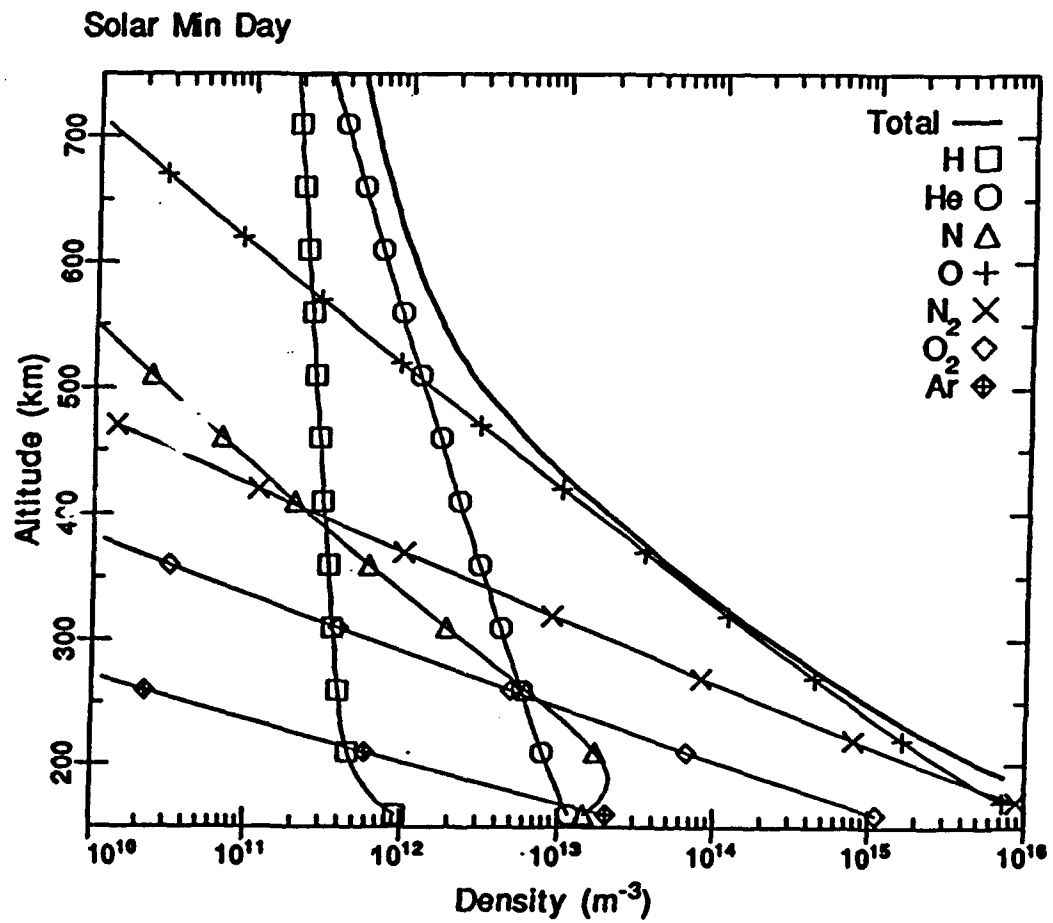


Fig. 2.10. The density of thermospheric constituents versus altitude during solar minimum at local noon.

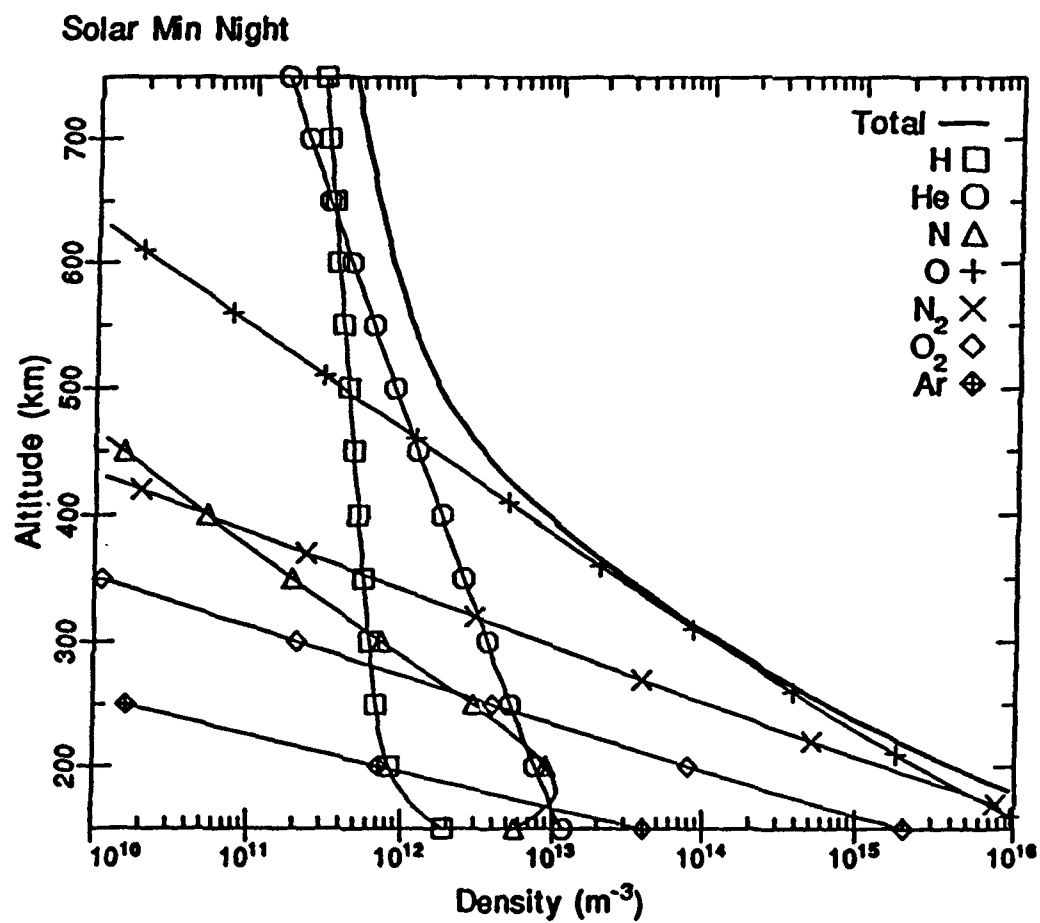


Fig. 2.11. The density of thermospheric constituents versus altitude during solar minimum at local midnight.

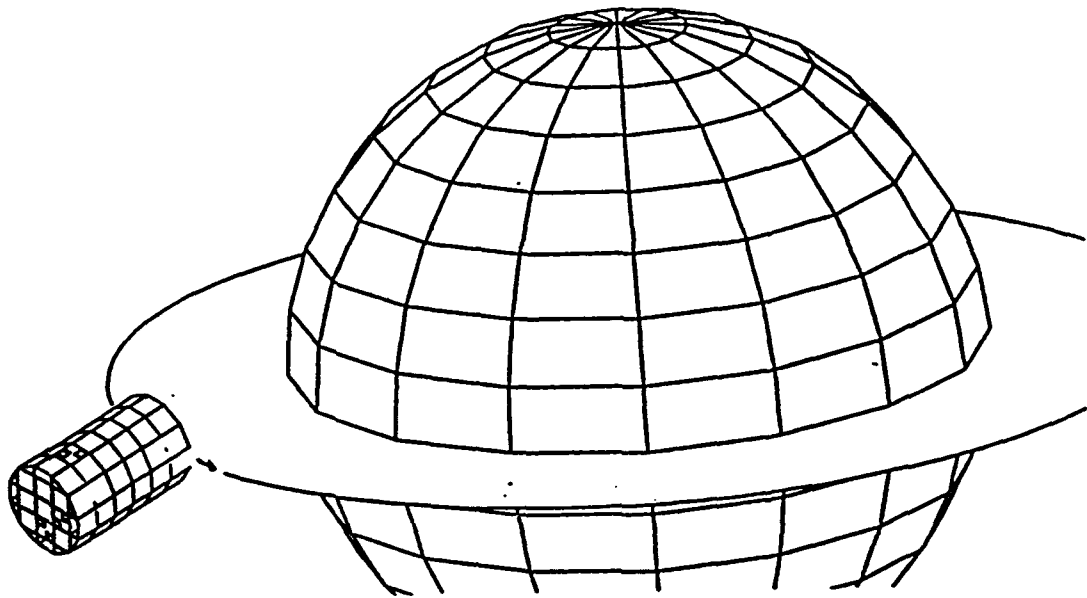


Fig. 2.12. The orientation of LDEF in orbit. North pole is visible, as well as six of the collectors of IGE.

so that the space end was always oriented to outer space. The orbit was stable. LDEF orbited about the earth much as the arrow of a clock hand revolves around the center of the clock.

Figure 2.13 depicts the various fields of view of the seven collectors relative to LDEF [Lind *et al.*, 1991]. The angles listed are defined in the YZ plane. The zenith angle of zero degrees is aligned spaceward. An angle of +90° is aligned down the positive Y axis. The +110° collector is shielded from interstellar gas particles by the Earth because it looks below the local horizon. This collector will field test the computational results of this paper. Besides the +24° and the +70° collectors, two collectors point below the plane of orbit, one at -24°, one at -70°.

The remaining two collectors were oriented in the XZ plane. Figure 2.14 diagrams the position of these collectors on the space end of LDEF. Collector three tipped 24° into the virtual wind created as LDEF orbited through a relatively stationary atmosphere. The second of this pair was tilted 24° out of the virtual wind. Together, this pair allowed measurement of atmospheric helium so that a differencing method could be used to solve for the atmospheric helium. That value may then be subtracted out of the total concentration. Figure 2.15 shows the location of tray F6 on the south

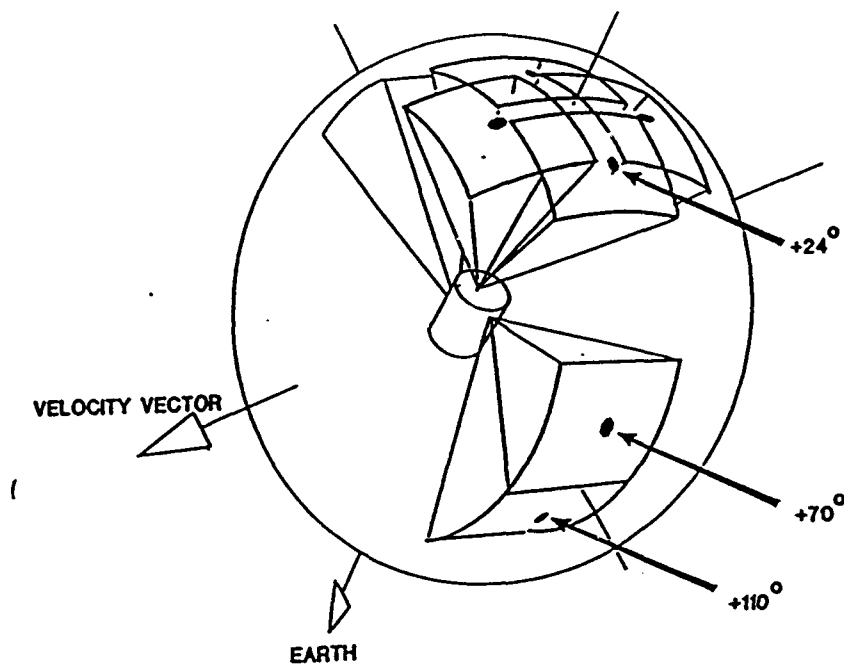


Fig. 2.13. The orientation of the fields of view of the seven IGE collectors relative to LDEF. Positive angles are to the north of the LDEF ground track. The $+110^\circ$ viewing direction was capable of collecting only atmospheric helium.

face and tray E12 on the north face of the spacecraft. Table 2.2 summarizes the position and viewing angles of all seven IGE collectors.

The individual trays held the collectors in place. The top of each collector opening was flush with the face of LDEF. For example, no part of the collector housing is exposed above the plane of the spacecraft. The trays on the spaceward face of LDEF, H6 and H9, were dimensioned exactly alike. Figure 2.16 shows the dimensions for a "glass" model of tray H6. The velocity vector of the satellite is to the right, as indicated by the coordinates. Collector three is tilted 24° into the wind, while collector two is tilted out of the wind. H9 was aligned 90° from tray H6, so the virtual wind passed over the tray baffle. This tray baffle, indicated in figure 2.16, was a thin strip of metal located at the top of the tray. The tray baffles restricted the fields of view of the collectors on the space end of LDEF. The background particles were obstructed from entry by the tray baffle over foil five. Another

Table 2.2 Collector Viewing Angles

Foil	View Angle	Tray	LDEF Side
1	-70° (S)	F6	South Face
2	0° (Aft)	H6	Spaceward
3	0° (Fore)	H6	Spaceward
4	+24° (N)	H9	Spaceward
5	-24° (S)	H9	Spaceward
6	+70° (N)	E12	North Face
7	+110° (N)	E12	North Face

look at figure 2.14 clarifies the orientation. The tray itself is boxlike, 85 cm long, 79 cm wide, and 30 cm deep.

The two remaining trays, E12 and F6, were also dimensioned alike, each on opposite sides of LDEF. Figure 2.16 illustrates the dimensions of tray F6, as well. The virtual wind passed across this tray from upper left, as shown by the coordinates. These trays are larger than those on the spaceward side, proportioned 124 cm long, 92 cm wide and 31 cm deep.

The most important determinant of the geometry of the IGE was the collector housing. Figure 2.17 displays the dimensions of one of these. All the collectors were identical to the one shown. The height from the top baffle to the foil was 38 cm. From a point at the center of the foil, the top baffle limits the field of view. The opening at the top baffle was a 30 by 30 cm square. The foils were centered at the base of the housing. The foils were square, 22 by 22 cm. This suggests a second helpful coordinate system.

The coordinate system most useful for the calculation of atmospheric helium accretion was founded at the midpoint of the foil. The positive X axis was defined as the velocity vector of the satellite as before. The Y axis was drawn at right angles to X and flush with the foil. The new Z axis was positive pointing out of the collector housing. The origin in this system, (0,0) was the foil midpoint. The center of the baffle opening was 38 cm above the foil origin and this point was exactly

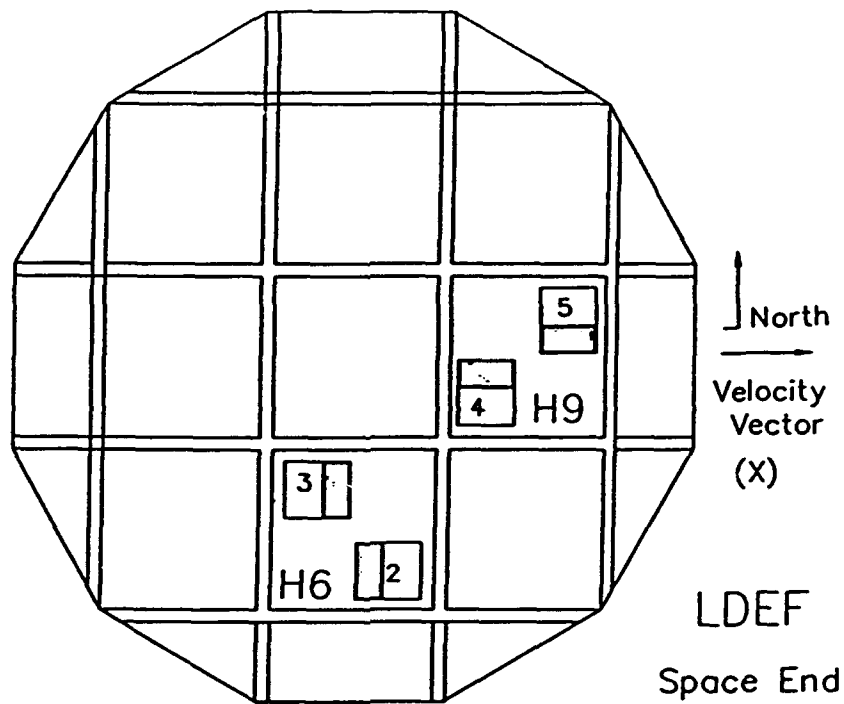


Fig. 2.14. The location of trays H6 and H9 on the spaceward side of LDEF.

15 cm to the midpoint of the top baffle along the X or Y axes. Therefore, the limiting angle for the field of view from the foil origin was the angle whose tangent was 38 over 15, along both axes. This angle was roughly 22 degrees from zenith.

In this configuration, for a particle to hit the foil origin, it must have a negative velocity in the Z direction, i.e., v_z less than zero. The particle must also have an angle of incidence between plus and minus 22 degrees in the XZ plane and the YZ plane. In three dimensions, this defines a field of view which is shaped like a four-sided pyramid as shown in figure 2.13.

This chapter has outlined the physical structure of the experiment, the parameters of the thermosphere, and the MSIS model. The following chapter covers the calculations required to determine the amount of atmospheric helium which accrued on the foils.

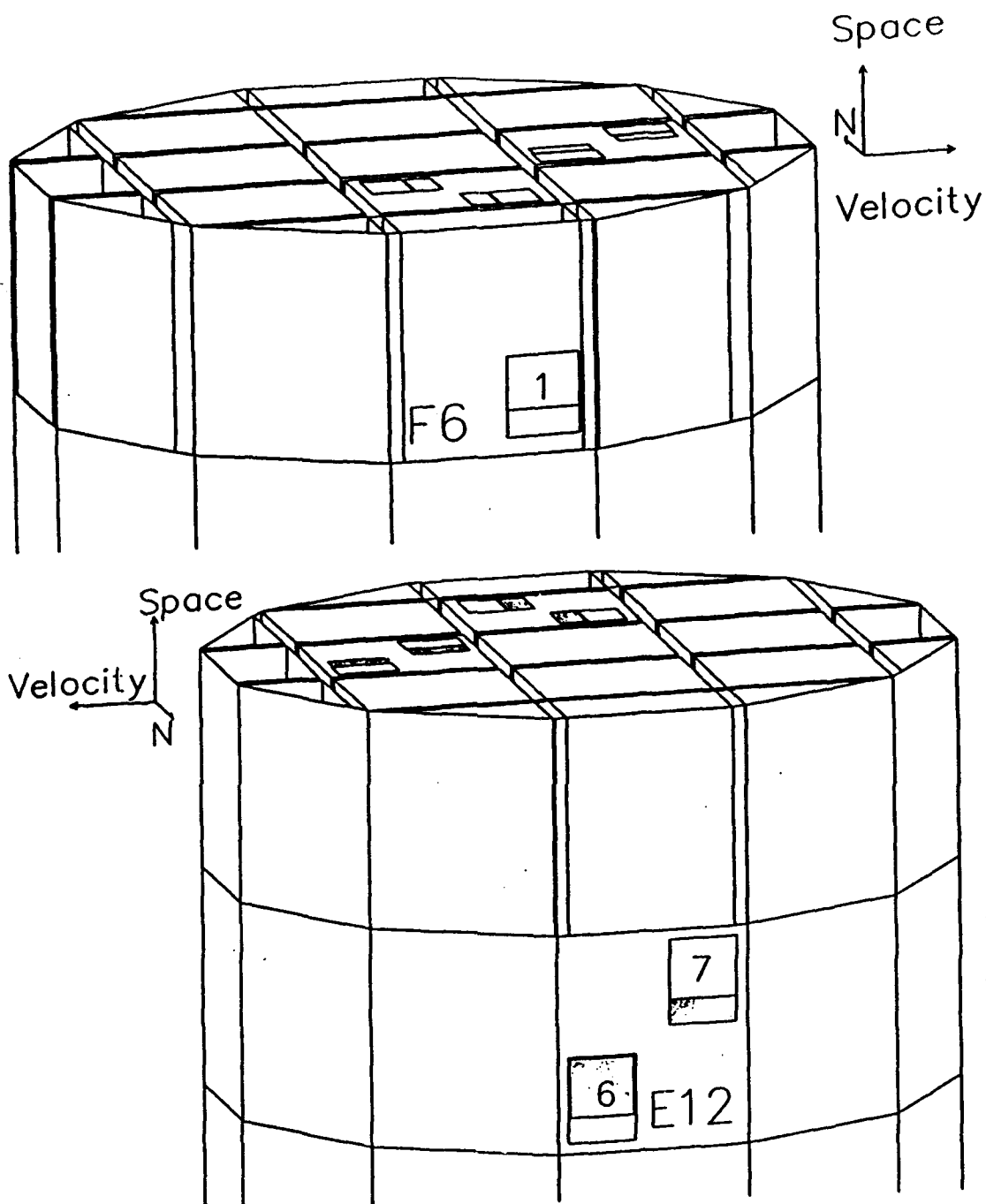


Fig. 2.15. The location of the collectors on the LDEF spacecraft. Above, the position of tray F6 on the south face. Below, the position of tray E12 on the north face.

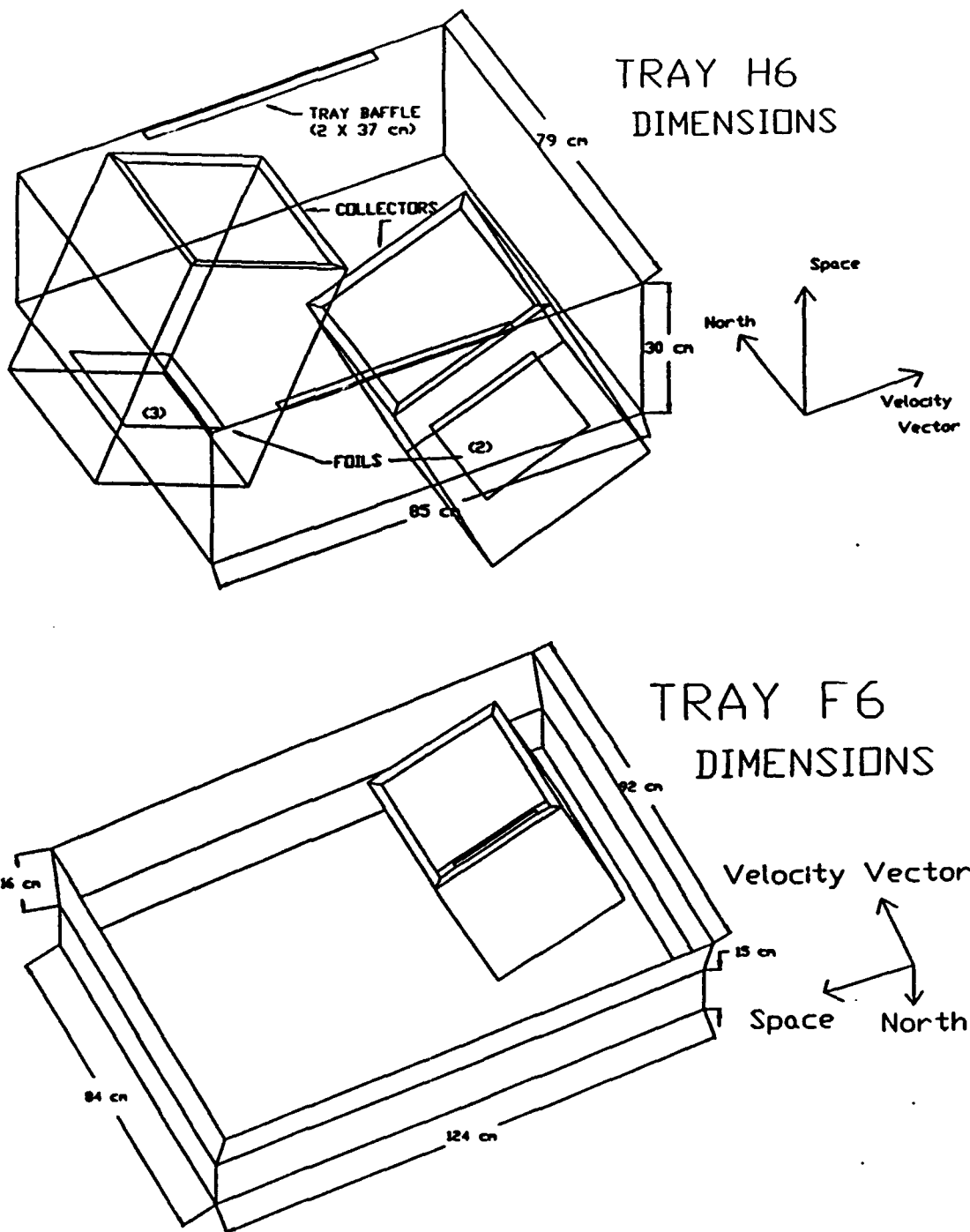


Fig. 2.16. The dimensions of tray H6 located on the spaceward side of LDEF, above, and the dimensions of tray F6 on the south face, below.

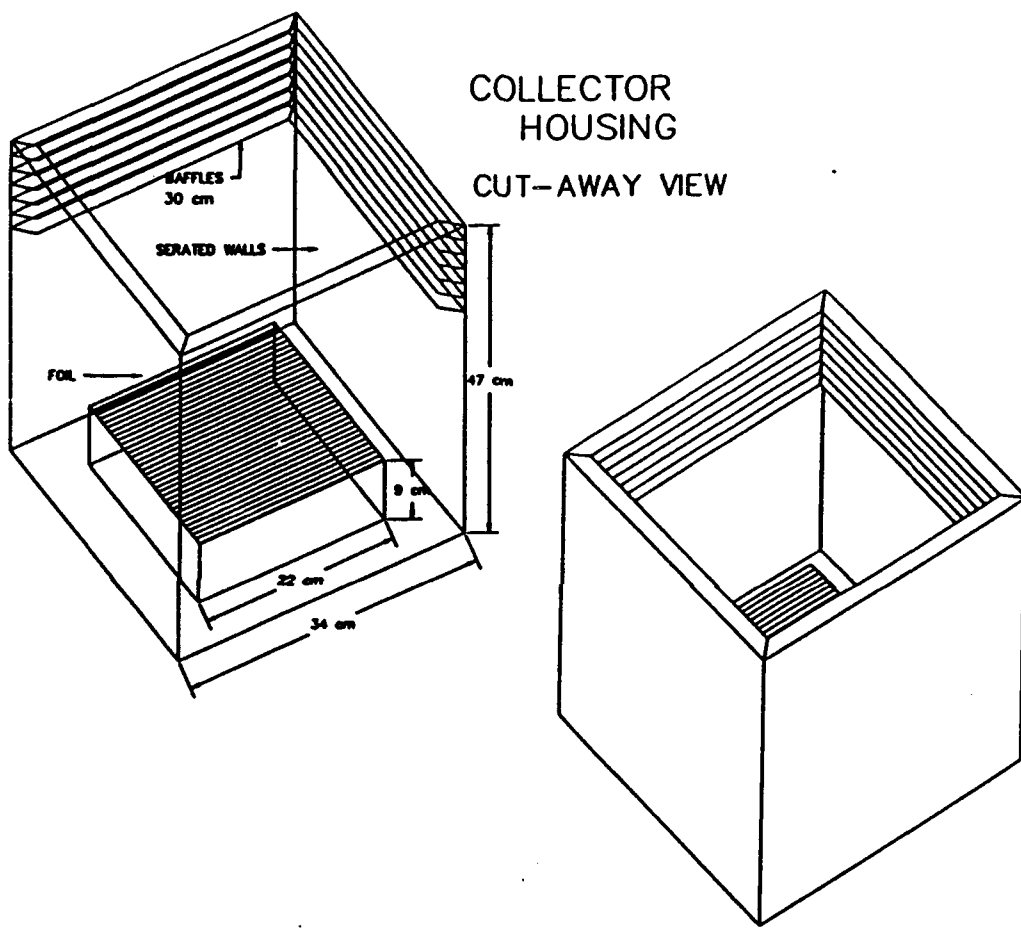


Fig. 2.17. The dimensions of each collector housing.

CHAPTER 3

CALCULATIONS

Chapter 2 dealt with the physical make-up of the Interstellar Gas Experiment and its orientation in three dimensions. The MSIS model was examined. Many figures providing expected ranges of thermospheric density and temperature were presented. This chapter will turn from the general to the specific. Chapter 3 will outline how the orbital motion was analyzed to get the necessary input for the MSIS model. It will then show how the MSIS figures of temperature and helium density were analyzed to solve for the actual accruement of helium particles on the foils.

3.1 Generating Input for the MSIS Model

The MSIS model was the source of the data needed to apply kinetic theory and acquire a solution to this problem. The ten specific parameters needed to run the model are year, day, second, altitude, geodetic latitude, geodetic longitude, local apparent solar time, a three-month average of F10.7 flux, daily F10.7 flux for previous day, and the daily magnetic Ap index. The first half of the problem was to provide this information for the entire six year flight of LDEF.

The duration of the flight was split into 70 month-long intervals, except for the first and last intervals, which were 22 days and 12 days, respectively. For the date input to the model, the midpoint of the interval was chosen. This generally meant the 15th of each month. The seconds parameter was chosen as midnight. The time input for MSIS is now fixed for the seventy intervals.

The problem became, given time, where was LDEF positioned? A review glance at table 2.1 shows that at launch, the altitude was 474 km and the right ascension at the ascending node (RAAN) was 228.4 degrees, with a precession rate of -6.8 degrees per day. The altitude of the satellite was monitored closely during 1989. At the time, no official recovery plans had been set. LDEF average orbital decay rates were published on a monthly basis. This data was interpolated to provide altitude

inputs for MSIS during each interval. Using similar information on the changing precession rate, a new RAAN was calculated for the midpoint of each month.

Surprisingly, the MSIS model is sensitive to different RAANs. If the RAAN input is altered to step around the globe, all other inputs being equal, the temperature and density varied because of the RAAN's effect on local solar time. By dividing RAAN by fifteen, it was converted to hours and added to the time of day to calculate the local apparent solar time. RAAN was used as the geodetic longitude for the MSIS input.

The RAAN was the starting longitude for one "typical" orbit. The geodetic latitude input was provided using the orbital inclination of 28.4°. Seven of the ten MSIS inputs are now set. The remaining three, the Ap magnetic activity, the F10.7 cm flux, and the three month average F10.7a cm flux, were accessed from archives at the National Center for Atmospheric Research.

Rather than take a onetime, one spot, surgical average for the entire month, I calculated a mean taken around the globe. This would preserve some of the spatial variance in evidence in figure 2.3. I modified an existing circular orbit code [*Thompson and Raitt, 1989*]. The code updated the seconds input, the LST input, the latitude, and the longitude every thirty seconds for a ninety minute orbit. MSIS was called 180 times, or every two degrees of longitude. The model returned three values of interest for each location, the total atmospheric density, the helium density, and the temperature. All values returned were for the altitude provided during that month.

To preserve some of the temporal variance present in figure 2.3, the temperature and density values were separated into two bins. One bin held local midnight to noon values, the other held local noon to midnight values. The ninety values in each bin were then averaged to produce one typical AM temperature and helium density, and one typical PM temperature and helium density. The results are plotted in figure 3.1 for the AM data. PM data is plotted in figure 3.2.

Other averaging schemes could have been adopted. The "two-a-day" method was chosen because the next step, the integration, becomes prohibitively slow. For example, the integration takes about 24 hours of calculation with two bins per day. Halving the interval to four per day, doubles the computation time.

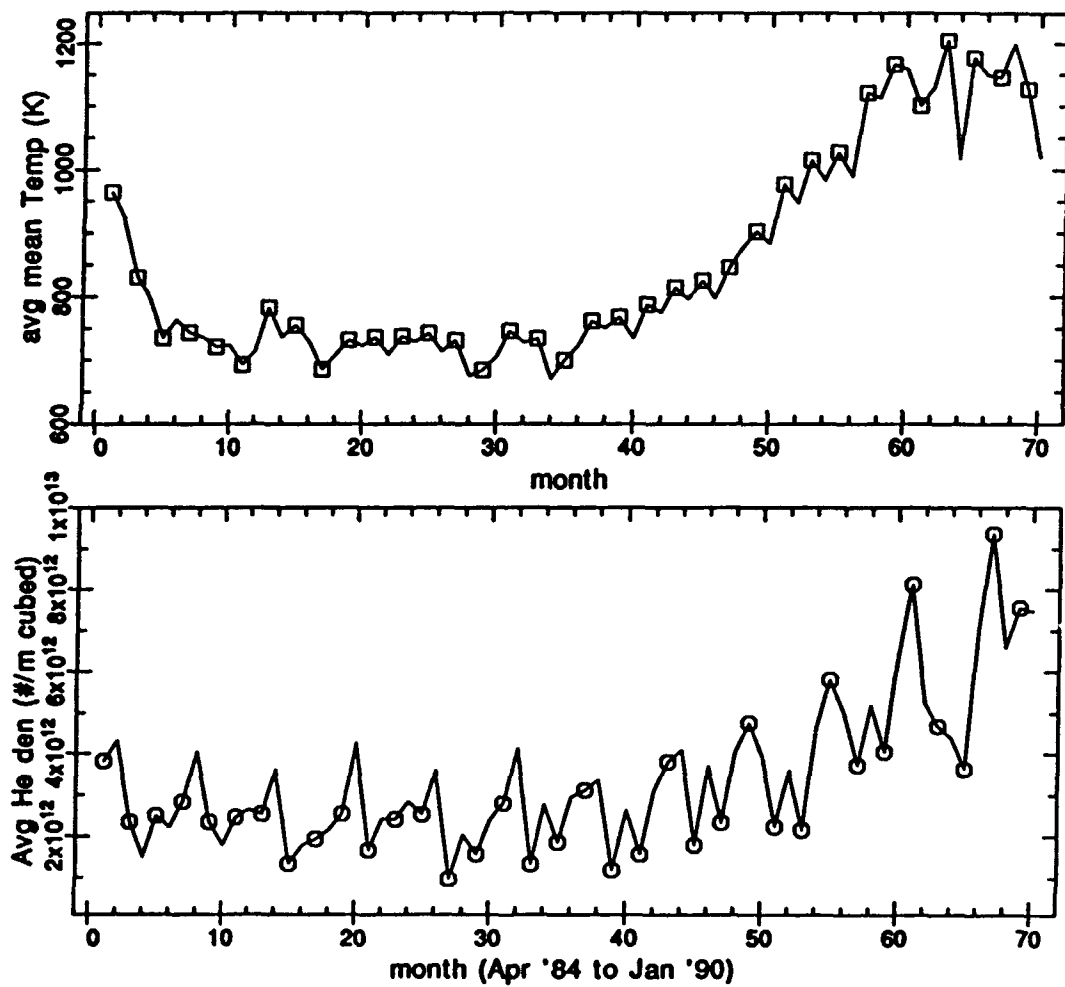
Avg AM Values at Mid-Month

Fig. 3.1. Average local AM values of temperature and helium density at LDEF altitude for the duration of the flight.

Avg PM Values at Mid-Month

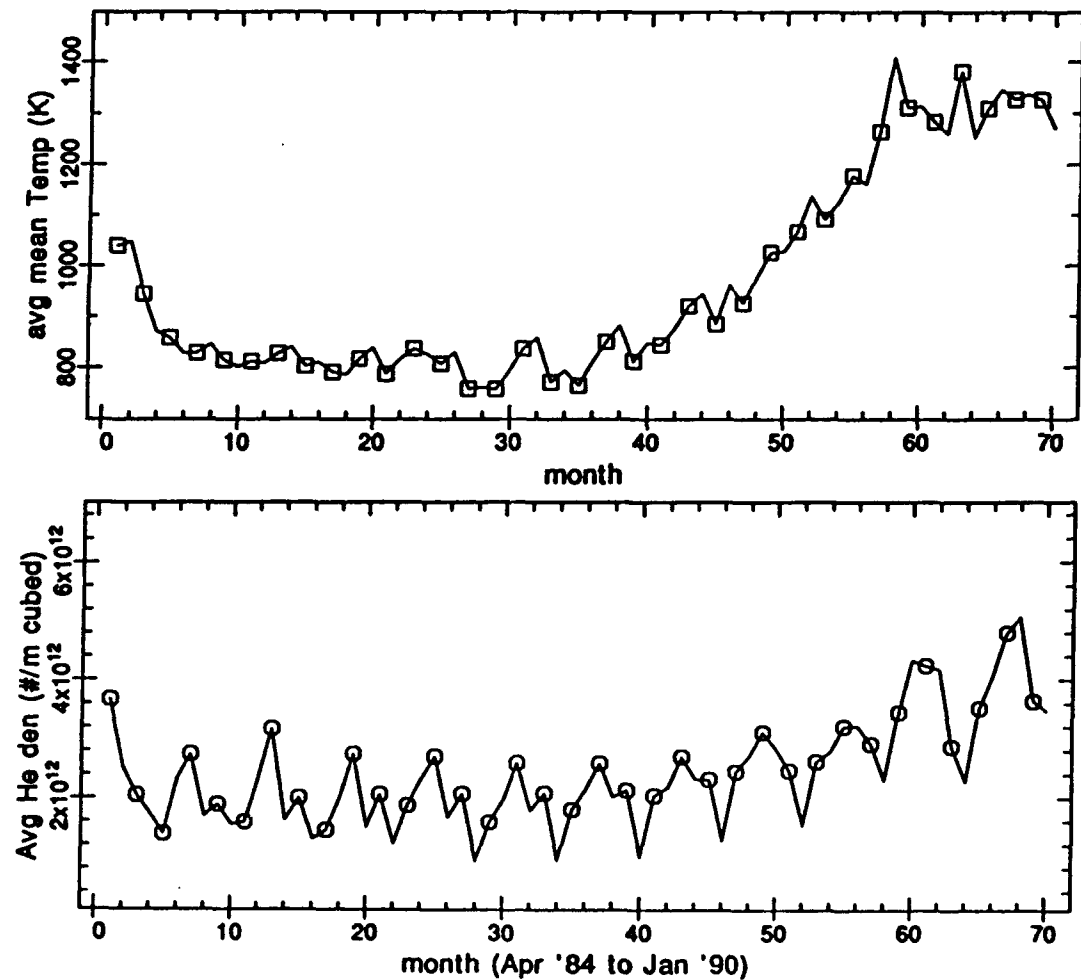


Fig. 3.2. The average PM values of temperature and helium density at LDEF altitude for the duration of the flight.

3.2 An Early Estimate

The results of the orbital averages from MSIS provided the parameters needed for the next step, the integration. The question of how many helium particles actually stuck to the foils after nearly six years in orbit could now be addressed. An extremely crude range of solutions was calculated using fluid theory.

Due to the geometry of the collector housing, no part of any foil was exposed to the virtual wind created by the spacecraft's flight. The inner housing baffles and serrations prevented any impingement of rebounding particles. Therefore, the results of fluid theory are the empty set, zero.

For an extreme upper limit, I assumed the foils were fully exposed perpendicular to the flow. Figure 3.3 displays some average information regarding the LDEF orbit. Figure 3.4 shows values of key thermospheric parameters at LDEF altitude, averaged over the entire 69-month period. Data from figures 3.3 and 3.4 was used for this "butterfly net" over estimation. The flux of helium particles was calculated by multiplying the orbital velocity times the He density. The number of particles collected on the foil was calculated by multiplying the flux times the total time in orbit. The result was roughly $4(10)^{24}$ helium particles per square meter of foil. This also assumes every particle will adhere to the foil. Clearly, fluid theory had to be abandoned, but the extreme limits it provided proved useful.

3.3 Application of the Kinetic Theory of Gases

The problem fits the principles of the kinetic theory of gases, pioneered by Ludwig Boltzmann and James Clerk Maxwell. The three basic assumptions required to apply this theory are first, that the gas has a large number of spherical particles which make elastic collisions with themselves. The thermosphere contains $3(10)^{12}$ helium particles per cubic meter, a reasonably large number. The second requirement assumes the helium molecules are separated by large distances relative to their own diameters. This condition is met considering the mean helium diameter is little more than 2

ORBIT FACTS

KEY DATES

Start: 7 Apr 1984, 10:26 MST
 Finish: 12 Jan 1990, 8:16 MST

MEAN ALTITUDE

456 km

MEAN ORBIT LENGTH

42900 km

MEAN LDEF VELOCITY

7641 m/s

TIME FOR ONE ORBIT

94 min

TOTAL NUMBER OF ORBITS

32250

TOTAL TIME IN ORBIT

69 months
 181864000 secs

Fig. 3.3. A summary of key facts of the LDEF orbit.

Angstroms, while the spacing between particles is roughly $7(10)^{-5}$ meters. Finally, the theory assumes that the molecules exert no forces on each other except through collisions. Helium is an inert gas which makes this assumption valid.

Given the above conditions, kinetic theory concludes that after some short time, the particles will come into a state of equilibrium with each other. The equilibrium distribution is the one that remains unchanged by elastic collisions. Maxwell also assumed the velocity components of each particle were independent. The result of this derivation was the velocity distribution function, equation 1.2.1, reprinted here. Again, this distribution function is defined so that $f(r,v,t)$ is the number of molecules at position $r + dr$, with velocity between v and $v + dv$, at time t .

THERMOSPHERIC FACTS

MEAN HELIUM DENSITY
 $2.9(10)^{12} \text{ m}^{-3}$

MEAN TEMPERATURE
 $911 \text{ }^{\circ}\text{K}$

PRESSURE
 $3(10)^{-10} \text{ Torr}$

MEAN FREE PATH
 1630 km

MEAN SQUARE SPEED
 $1.9(10)^6 \text{ m}^2/\text{s}^2$

MEAN SPEED
 2190 m/s

ROOT MEAN SQUARE SPEED
 2375 m/s

Fig. 3.4. A summary of typical thermospheric parameters at orbit altitudes, averaged over the entire 69-month flight of LDEF.

$$F(v_x v_y v_z) = f(v_x)f(v_y)f(v_z) = (m/2\pi kT)^{3/2} \exp(-mv^2/2kT) \quad (1.2.1)$$

Where m is the mass of the particle, T is the temperature, k is Boltzmann's constant, and v is the velocity of the particle. By integrating the Maxwell-Boltzmann velocity distribution function over all possible velocities, every helium particle is accounted for.

The assumption of thermal equilibrium implies any position r of given altitude is similar to the next. It also means that changes in time are slow enough to be treated as a constant of the integration. The problem is reduced from one with seven variables to one with three velocity variables. By transposing the geometry of the collector housing into velocity space with certain fields of view, the stage is set to solve for the number of particles which hit the foil.

3.4 A Spherical Coordinates Estimation

Spherical coordinates seemed like a useful approach at first. Some error would be introduced by rendering the actual geometry into spherical geometry. The rectangular opening of the housing was approximated by a circular opening of equal area. The field of view went from a pyramid to a cone. The advantage of the spherical coordinates is the limits of integration are very straight forward.

The coordinate system was aligned as described above. The origin was the center point of the foil. The Z direction was perpendicular to the foil, positive being upward. The X direction was oriented positive towards the direction of motion. The angle phi was measured from the v_x axis. The angle theta was measured from the v_z axis.

The derivation of the Maxwell-Boltzmann velocity distribution function into spherical coordinates is outlined here. The equation for a drifting Maxwellian was:

$$v^2 = (v_x - v_{x0})^2 \hat{x} + v_y^2 \hat{y} + (v_z - v_{z0})^2 \hat{z}$$

The v_{x0} and v_{z0} are constants due to the orbital velocity of the spacecraft. They were defined:

$$v_{x0} = v_{\text{orb}} \cos \Psi$$

$$v_{z0} = v_{\text{orb}} \sin \Psi$$

The angle psi was defined as the angle from zenith, or space direction, to the Z axis normal to the foil, in the XZ plane. Psi equaled zero for all collecting foils except foils two and three, where psi equaled -24° and 24° , respectively.

The velocity equation for the drifting Maxwellian was transformed using the following set of substitutions.

$$v_x = r \sin\theta \cos\phi$$

$$v_y = r \sin\theta \sin\phi$$

$$v_z = r \cos\theta$$

The unit direction vectors were substituted as follows:

$$\hat{x} = \sin\theta \cos\theta \hat{r} + \cos\theta \cos\phi \hat{\theta} - \sin\phi \hat{\phi}$$

$$\hat{y} = \sin\theta \sin\phi \hat{r} + \cos\theta \sin\phi \hat{\theta} + \cos\phi \hat{\phi}$$

$$\hat{z} = \cos\theta \hat{r} - \sin\theta \hat{\theta}$$

After much algebra, it can be shown that the expression for velocity squared in spherical coordinates is equation 3.2.1.

$$v^2 = v_r^2 + v_{\theta}^2 + v_{\phi}^2 - 2v_r(v_{\theta}\sin\theta\cos\phi + v_{\phi}\cos\theta) \quad (3.2.1)$$

The Maxwell-Boltzmann velocity distribution function becomes:

$$f(v_r, \theta, \phi) = C_n \exp(-(v_r^2 + v_{\theta}^2 + v_{\phi}^2 - 2v_r(v_{\theta}\sin\theta\cos\phi + v_{\phi}\cos\theta))/v_m^2)$$

The thermal velocity is defined as:

$$v_m^2 = 2kT/m$$

As before, k is Boltzmann's constant, T is the temperature, and m is the mass of the helium particle.

The constant C_n is defined as:

$$C_n = (1/\pi v_m^2)^{3/2}$$

This distribution function was integrated as follows:

$$\iiint_R f(v_r, \theta, \phi) v_r^2 \sin\theta dv_r d\theta d\phi$$

The limits of phi were 0 to 360°. Theta ranged from 0 to 22°. The velocity extended from 0 to 20 km/s.

The probability of the particle adhering to the foil is a function of v_r . The spherical coordinates method was deserted because of the dependence with velocity. This dependence required the Maxwellian to have no bulk drift. Then the limits of integration would be dependent on the orbital velocity. These limits proved to be elusive.

Despite this, I ran the spherical calculation. I assumed the temperature and helium density were the mean values of figure 3.4. The probability of sticking to the foil was estimated at 100 percent. The flux was calculated by multiplying the integrand by the Z component of v_r . The final result was multiplied by total time in orbit. This rough estimate yielded a result of $2(10)^{18}$ particles per square meter of foil. This result was expected to be an overestimate.

3.5 The Probability of a Particle Adhering to the Foil

The beryllium-copper foil's trapping probability was tested by the IGE team in the early 1980's. The results were directly related to the particle velocity. Table 3.1 contains the results of this test. For the purposes of the calculation, I needed a continuous function that fit this data for any particle velocity.

The probability data was represented using a group of five functions, one for five different ranges of velocity. The coefficients were adopted using a weighted least-squares method. The equations are presented here. For velocities less than 20 km/s:

$$\eta_1 = (10)^{-15} e^{(v/1000)} / (1 - 5(10)^{-5}(v-1000))$$

For velocities between 20 and 25 km/s:

$$\eta_2 = v^2(10)^{-13} / (1 - 1.932(10)^{-4}(v-20000))$$

Table 3.1 IGE Trapping Probability, The Eta Function

VELOCITY (km/s)	ETA
00	0.0
05	---
10	---
15	---
20	$1.0(10)^{-5}$
25	$4.6(10)^{-4}$
30	0.0030
35	0.0083
40	0.017
45	0.03
50	0.05
55	0.079
60	0.12
65	0.157
70	0.195
75	0.23
80	0.26
85	0.295
90	0.33
95	0.37
100	0.40

For velocities between 25 and 55 km/s:

$$\eta_3 = (2 v^2 / 1.16(10)^{10})(1-w) + (.00188 v^2 / 4.1(10)^9)w$$

where w is defined as:

$$w = 1 - 4(10)^{-5} (v - 25000)$$

For velocities between 55 and 60 km/s:

$$\eta_4 = v^2(10)^{-10} / 4(1 - 5(10)^{-5}(v-55000))$$

For velocities greater than 60 km/s:

$$\eta_5 = v^2 / 2.44(10)^{10}$$

The results of this fit are plotted in figure 3.5. The fit is reasonable. A note of caution, however, the data was unfortunately sparse below 20 km/s. The fit assumed an eta value of zero at

zero velocity. The next available data point was the value 10^{-5} at a velocity of 20 km/s. The value of the distribution function is a maximum at zero, but its value at 20 km/s is only 10^{-46} for a thermal velocity based at the mean temperature of 911 °K. Thus, this function was the greatest source of uncertainty in the entire calculation.

3.6 The Calculation in Cartesian Coordinates

3.6.1 The Limits of Integration

The next step was to find the limits of integration for the Maxwell-Boltzmann velocity distribution function, using velocity space. The concentric circles of figure 3.6 represent an ideal gas in thermal equilibrium with zero bulk flow velocity. The solution of the velocity distribution function is represented by concentric circles centered at the origin. The diagram is two dimensional in velocity space. LDEF cuts through this distribution with a velocity of 7.6 km/s along the v_x direction. Using the coordinate system outlined in section 2.4, where X is the direction of orbital motion, and Z is perpendicular to the foil face, then any foil except casettes two and three, can be represented by the point, ($v_x = 7.6$, $v_y = 0$, $v_z = 0$ km/s). This argument also neglects the yaw of 8°. If a particle has a velocity of (7.6,0,-1), it is capable of hitting the foil. Alternatively, if any particle has a positive v_z component, it can never hit the foil.

The limits in v_x depend on v_z , the same way that the distance from the center of the foil to the housing baffles depends on Z over X. So the field of view in the XZ plane is determined by the slope of the line, theta one, connecting the midpoint of the foil, to the midpoint of the top aft baffle. The equation for this line is:

$$v_z = \theta_1(v_{zx} - v_{xp})$$

The line connecting the midpoint of the foil to the midpoint of the top fore baffle is given by:

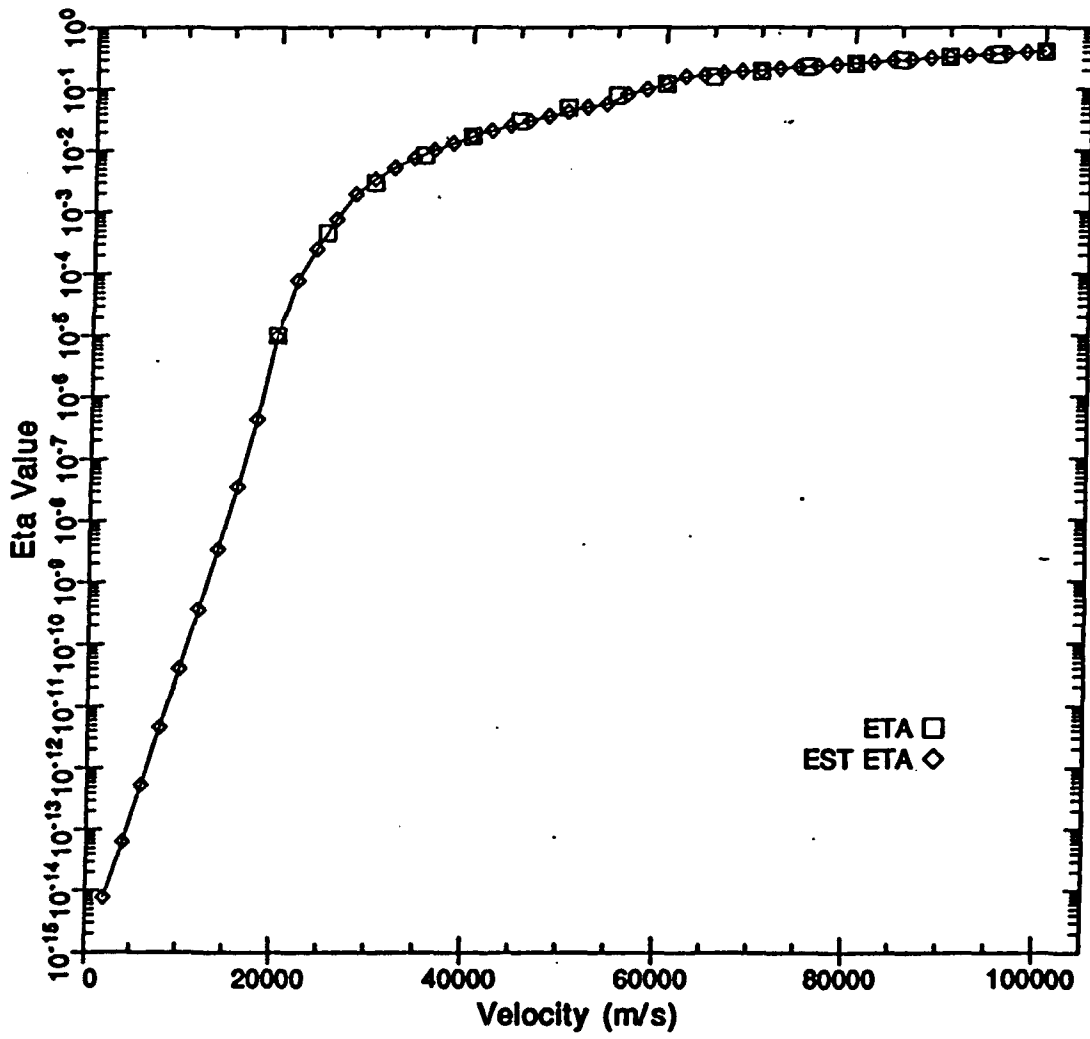


Fig. 3.5. The trapping probability η , as a function of velocity. The boxed data points are experimental results, the diamond points are calculated estimates.

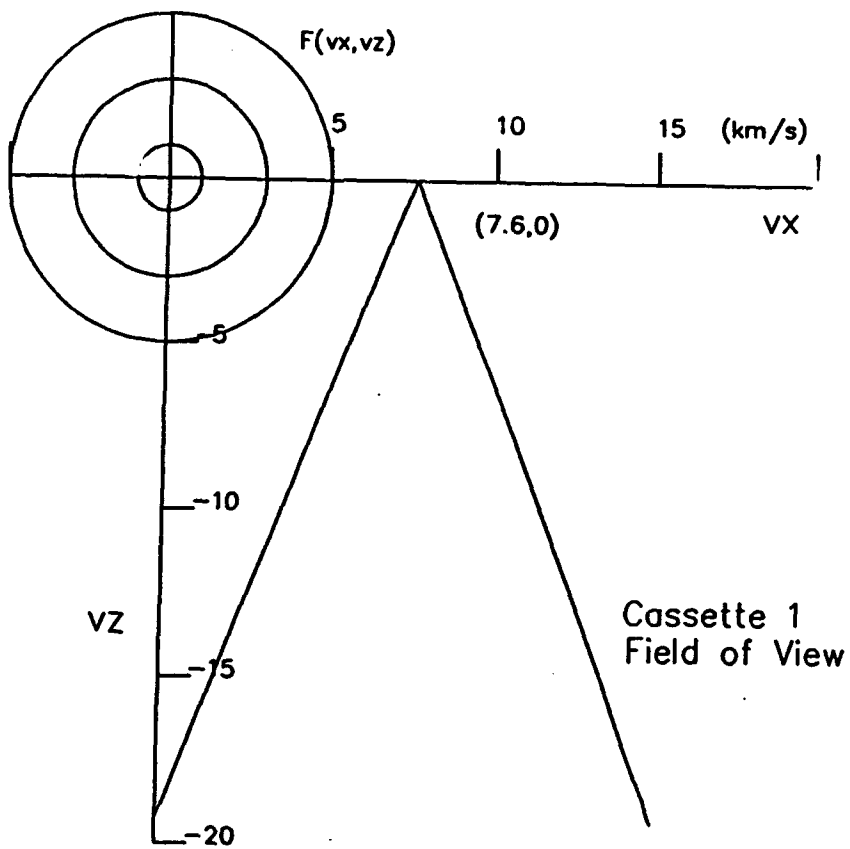


Fig. 3.6. Lines representing the field of view for the midpoint of the foil on collectors oriented normal to the direction of motion.

$$v_z = \theta_2 (v_{z0} - v_{zo})$$

Theta one and theta two were allowed to vary during the integration procedure. In effect, the slopes changed as the position on the foil changed. This allowed the calculation of the density gradient across each foil. The two lines intersect the v_x axis at the orbital velocity of LDEF, v_{zo} :

$$v_{zo} = v_{orb} \approx 7600(\text{m/s})$$

The region is closed by the line at the Z velocity cutoff. For most calculations the greatest v_z chosen was 15 km/s. In general, the region representing the field of view was a triangular wedge as shown in figures 3.6 to 3.8.

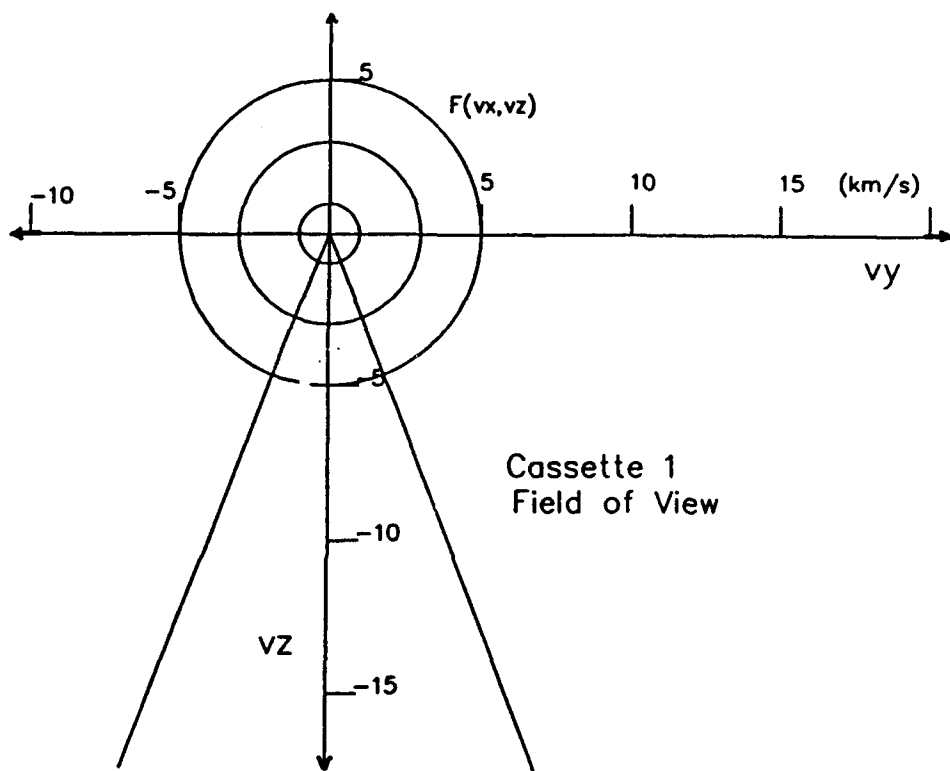


Fig. 3.7. Lines representing the field of view of all collectors oriented normal to the direction of motion in v_x , v_z space, neglecting the yaw of 8° .

The situation is analogous in the YZ plane, with minor variations. For the five collectors oriented normal to the X direction the slope of the field of view was also 38 units up, 15 units over. These slopes were defined as phi one and phi 2. Neglecting a slight yaw of 8° , there was no bulk drift in the Y direction so the equations defining the field of view in velocity space were:

$$v_z = \phi_1 v_{yx} ; \quad v_z = \phi_2 v_{yx}$$

The velocity distribution function proved to be symmetric with respect to the v_y direction, as shown in figure 3.7. That fact enabled the integration to extend from zero to the line with slope phi one, while multiplying the sum by a factor of two. The result of the limits of integration was a three-dimensional field of view shaped like the four-sided pyramid of figure 2.13.

The limits of integration were slightly different for collectors two and three. These collectors were oriented with an angle psi equal to 24° in the direction of motion. The lines representing the

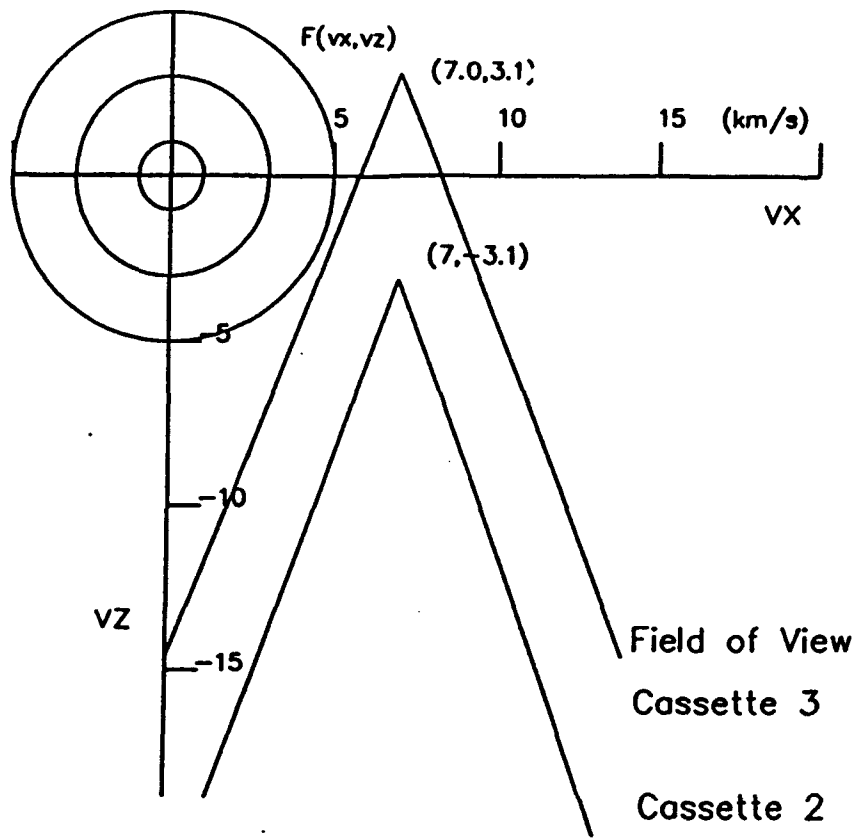


Fig. 3.8. Lines representing the field of view for collector three on tray H6.

field of view intersect at the point ($v_x = v_{x0}$, $v_y = 0$, $v_z = v_{z0}$). These fields of view are graphed in figure 3.8.

3.6.2 Calculating a Density Gradient Across Each Foil

The limits of integration were altered to represent different positions across the foil. The arguments of the section above all describe the field of view at the midpoint of the foil. The slopes were always 38 cm up to 15 cm over, in both the XZ plane for theta, and the YZ plane for phi.

To calculate the number of particles which could see the foil at any position on the foil, I altered the slopes to represent the limiting angles for the new position. I divided the foil into 25 squares. From the midpoint of each of these squares I recalculated the slopes. These new slopes

became the limits of the integration. After a test integration, the data showed there was no change in particle density across the foil in the Y direction.

This simplified the calculation. The foil was divided into five strips parallel to the Y axis. The slope, phi 1, used for each strip, was fixed at -38/15. Physically this represented the X axis, the centerline of the foil. Assuming the origin is at the foil midpoint, the points integrated to determine the density gradient across the foil were:

$$(-8.9,0), (-4.4,0), (0,0), (4.4,0), \text{ and } (8.9,0)$$

The points above were the midpoints of the foil regions which I numbered 1, 2, 3, 4, and 5, respectively. Figure 3.9 illustrates the changing field of view across the foil, on the v_x - v_z grid.

3.6.3 The Integration Limits Including the Yaw of 8°

When LDEF was deployed, the spacecraft was placed into orbit rather gingerly because any spin or wobble introduced would take a while to stabilize. The shuttle crew did an excellent job of launching LDEF, however, the satellite was twisted around the Z axis with an angle of 8° to the right for an observer facing in the negative Z direction. This slight twist is called a yaw. The crew opted to accept this yaw rather than risk introducing a more serious orbital flaw during a correction.

The yaw affects the limits of integration. The intersection of the lines representing the field of view were now changed. The yaw introduced a factor of sine and cosine of eight degrees, multiplied by the LDEF orbital velocity of 7.6 km/s.

For example, consider foil cassette 4, on tray H9, on the space side of LDEF. In velocity coordinates (v_x, v_y, v_z) , the old intersection of the fields of view was $(7.6, 0, 0)$ km/s. The new intersection accounting for the yaw was $(7.5, 1.0, 0.4)$ km/s. The yaw skewed the particle distribution on the foils from lines of constant density which ran parallel to the Y axis to lines with a slope of eight degrees. This yaw slightly alters the flux on all foils.

There remains one singularity. The tray baffle described in section 2.4 partially obscured the view of collector five, also on tray H9. Only the southwest sector of the foil was affected by this tray baffle. The calculation for this section of the foil needed a change of slope for theta 2, in the XZ

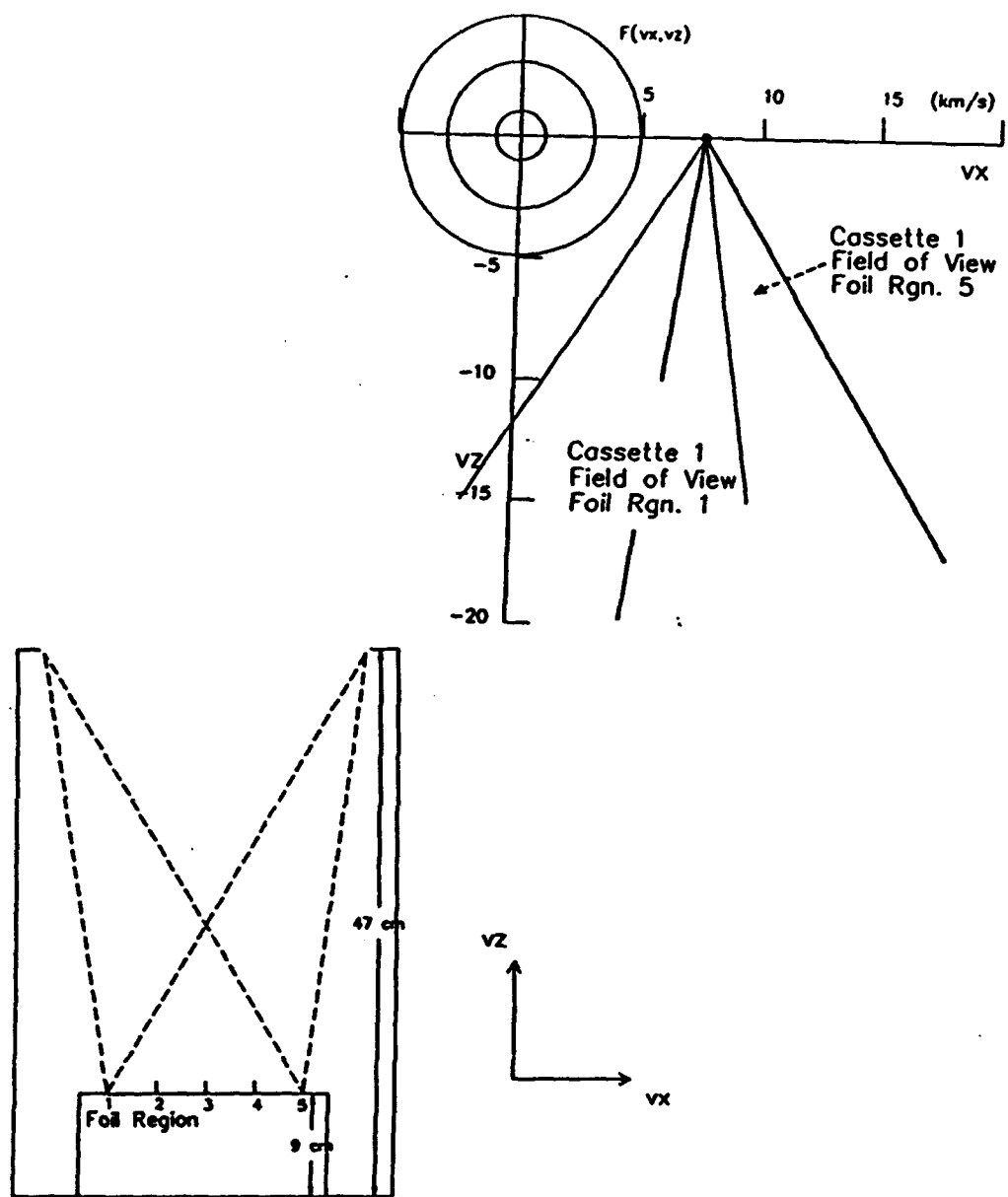


Fig. 3.9. A profile of a foil collector housing. The foil cassette is visible at the base. The dashed lines represent the field of view for foil region 1, the downwind side of the foil, and for foil region 5, the upwind side.

plane, to account for the limiting angle of the tray baffle.

3.6.4 The Numerical Solution

All the elements were now in place to perform the integration. The numerical method used was the rectangle rule in three-dimensional velocity space. Below is a description of the program that performed the integration.

First I selected a low limit for the Z component of velocity. I chose this limit as -15 km/s because the solution to the distribution function at this range is an extremely low $1(10)^{-26}$. Any contribution to the final sum from the velocity space outside this range would be insignificant. With this limiting Z component, the program used the equations presented in section 3.6.1 to determine the upper and lower limits of integration in the X and Y components of velocity.

The program was segmented to calculate two sums per month, an AM sum using the temperature and density values from figure 3.1, and a PM sum with the data from figure 3.2. To do this, the program read values for the month number, the seconds per month, LDEF orbital velocity, as well as the temperature and helium density data supplied by MSIS. For each month, this data was used to calculate a new thermal velocity, and a new normalization constant, C_n . The new orbital velocity value was used to redetermine v_{x0} and v_{z0} . Another loop provided new slopes, theta 1 and theta 2, to represent differing fields of view for five different points on the centerline of each foil.

Next, I selected a small increment dv. The smallest velocity interval chosen was 50 m/s. This defined a cubic increment in velocity space. The program stepped through the entire range of velocity space within the limits of integration. With each step the program tested whether a particle with the specific X, Y, and Z components of velocity could hit the foil. If the particle could hit the foil, the program called the velocity distribution function and the eta function. These two probabilities were calculated with the specific velocity which could hit the foil, and then multiplied together. Also multiplied to this, was the value dv^3 times the Z component of velocity. These partial products were summed at each step.

With the limits of integration represented in km/s, the integration equation looked like:

$$\text{Flux} = \rho_{\text{He}} \int_{-15}^0 \int_0^{-4v_z} \int_{4(v_z-19)}^{-4(v_z-19)} F(v) \eta(v) v_z dv_x dv_y dv_z$$

ρ_{He} was the helium density in particles per cubic meter. The eta function was described in section 3.5. $F(v)$ was defined as:

$$F(v) = f(v_x)f(v_y)f(v_z) = (m/2\pi kT)^{3/2} \exp(-mv^2/2kT)$$

The units for the flux term are helium particles per square meter per second. Figure 3.10 plots the results. The error estimate is based on uncertainties in MSIS output. The basic source of the uncertainty was a plus or minus 50 °C on temperature, and plus or minus 30 percent on helium density [Hedin *et al.*, 1974]

The final sum was multiplied by half of the seconds per month. The seconds were halved because this was done for AM and PM data. After the normalization constant, C_n , and the helium density were multiplied in, the AM monthly total was added to the PM monthly total for a final result for that month. Lastly, each month's subtotal was summed together for a final result with units, helium particles per square meter of foil surface. Figure 3.11 displays a three-dimensional view of the gradient of helium density across the foils.

When the yaw is factored into the calculation, the results are skewed eight degrees. Figure 3.12 displays a three dimensional profile of the helium density with respect to position on the foil. These results were calculated for foil cassette 4.

A review glance at figure 2.16 shows the tray baffle on tray H6. A similar tray baffle on tray H9 effected the distribution on foil cassette 5, because the virtual wind flowed across this baffle. On the south side of the downwind portion of foil 5, the tray baffle limited the field of view. Figure 3.13 shows a profile of the helium density with respect to foil position for foil 5. Notice how this figure compares with figure 3.12. The southwest sector of the foil has decreased helium density because the tray baffle intercepted particles which were free to hit the other foils.

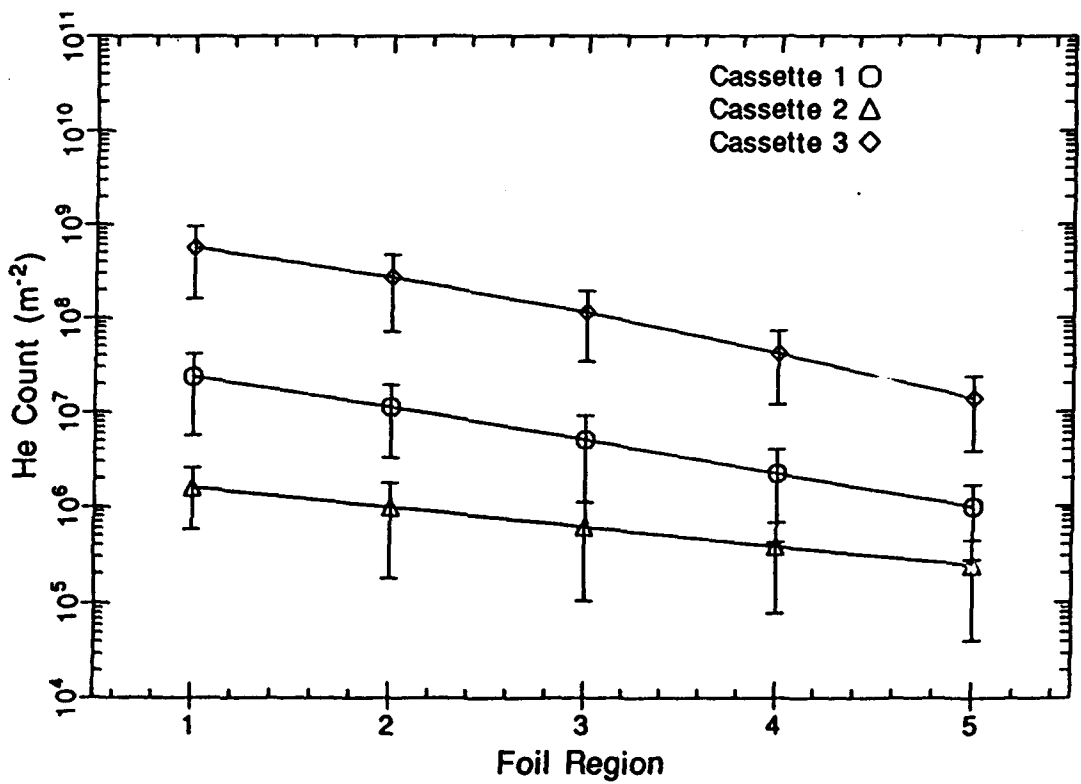


Fig. 3.10. The helium particle density on the foil after LDEF's flight. First data point is on the downwind side of the foil, last data point is on the upwind side of the foil.

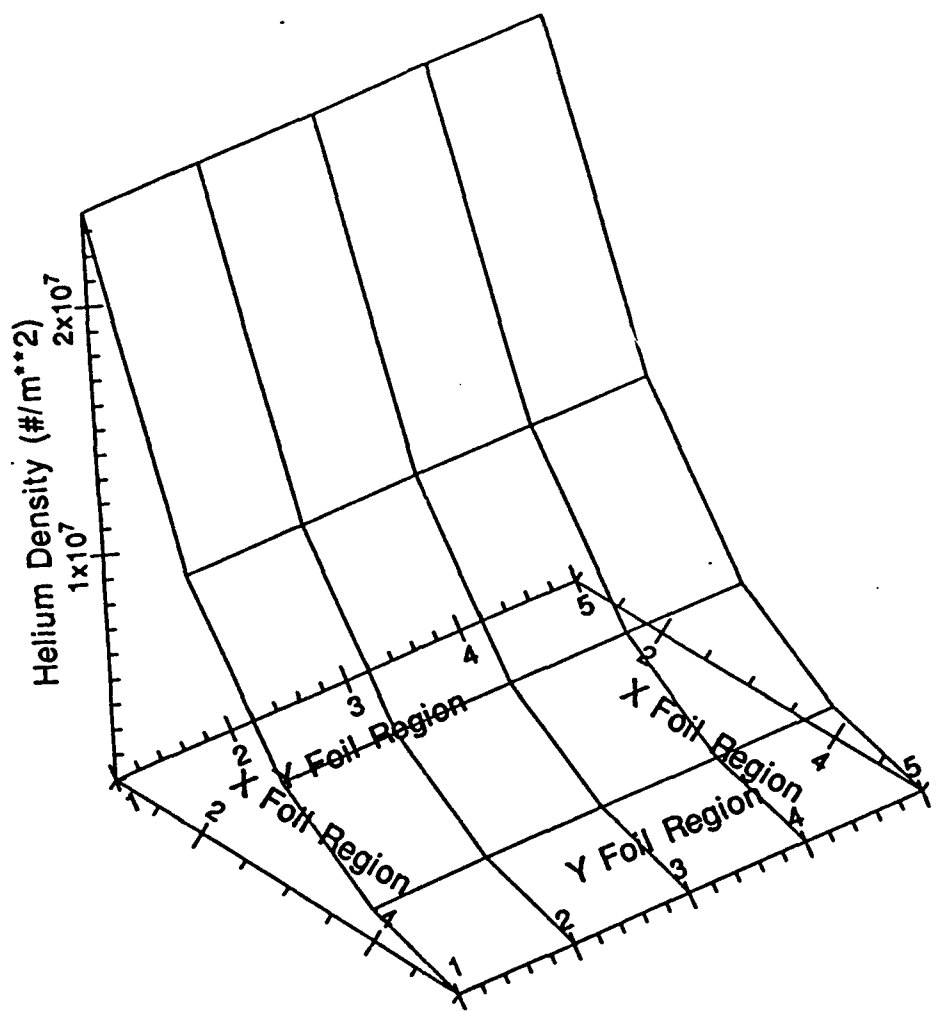


Fig. 3.11. A three-dimensional plot of the helium density gradient across the foils, neglecting the 8° yaw.

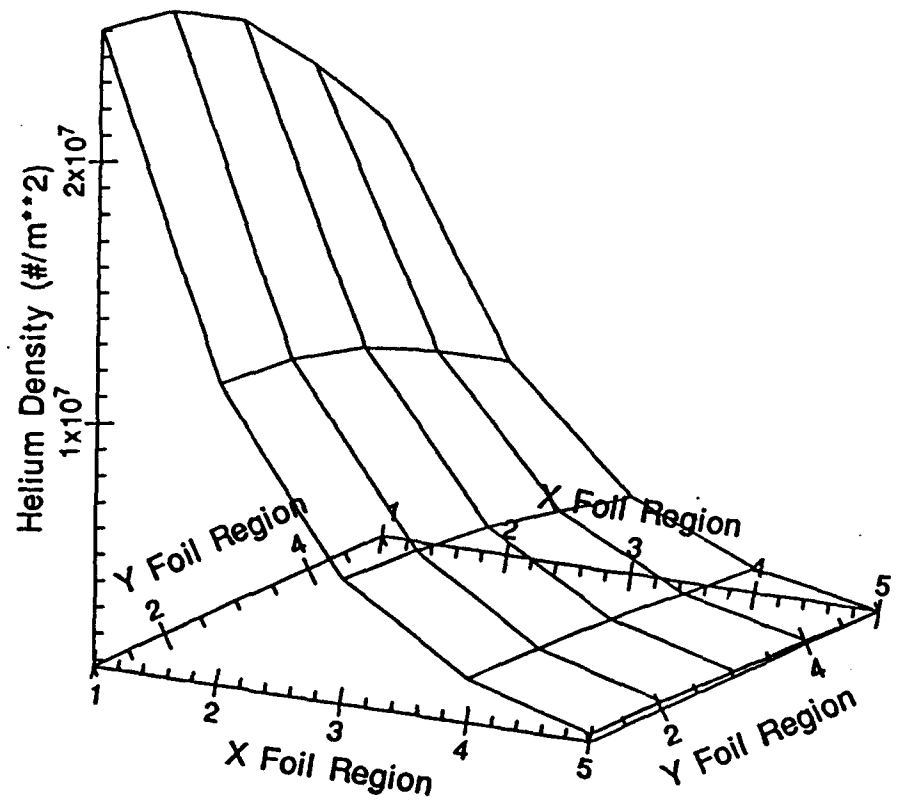


Fig. 3.12. A three-dimensional representation of the helium density found on foil cassette 4 including the yaw. This applies to foils oriented perpendicular to the orbital velocity.

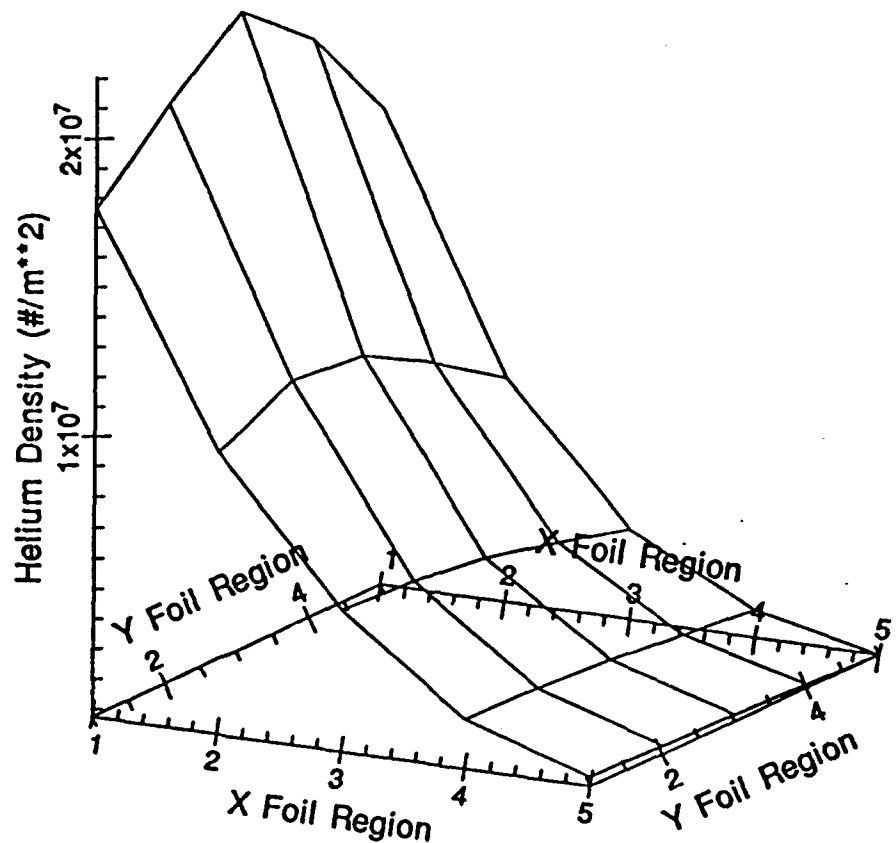


Fig. 3.13. A three-dimensional display of helium density with position on foil cassette 5. This distribution includes the eight degree yaw and the effect of the tray baffle on the upwind side of tray H9.

3.7 The Error Function Solution

Dr W. Schmickler proposed the following method to solve the problem. The method applied the error function defined as:

$$\operatorname{erf}(x) = 2/\sqrt{\pi} \int_0^x e^{-z^2} dz$$

This is similar in form to the foil calculation, which in one dimension may be written as:

$$f(v) = \sqrt{1/\pi v_{th}^2} \int_a^b e^{-(v/v_{th})^2} dv$$

If I redefine v/v_{th} as u , then $dv = v_{th} du$. Substituting these values into the equation above yields:

$$f(v) = \sqrt{1/\pi} \int_{av_{th}}^{bv_{th}} e^{-u^2} du$$

The v_{th} factor introduced by the u-substitution cancels the v_{th} squared term inside the radical.

Now by definition of the error function, $f(v)$ becomes:

$$f(v) = 1/2 [\operatorname{erf}(b/v_{th}) - \operatorname{erf}(a/v_{th})]$$

As before, this substitution cancels the factor of square root pi. That finished the development of the error function method in the one-dimensional case.

The integration for the foils was in three-dimensional velocity space. The transformation of the numerical integration equation of section 3.6, into the error function case is sketched below.

The limits of the integration had to be expressed in terms of v_z . Therefore, the error function substitution was done only for the v_x and v_y components of the velocity. The v_z component was left to vary as before from -15 km/s to 0 km/s in increments of dv_z . This method transformed the flux equation from:

$$\text{Flux} = \rho_{he} \int_{-15}^0 \int_0^{-4v_z} \int_{-4(v_z-19)}^{-4(v_z+19)} F(v) \eta(v) v_z dv_x dv_y dv_z$$

where:

$$F(v) = f(v_x)f(v_y)f(v_z) = (m/2\pi kT)^{3/2} \exp(-mv^2/2kT)$$

into:

$$\text{Flux} = \rho_{\infty} C_n \int_{-15}^0 \exp(-v_z^2/v_{th}^2) \eta(v_z^2 + v_{xo}^2)^{1/2} \alpha(v_z) v_z dv_z$$

C_n is the normalization constant:

$$C_n = (1/\pi v_{th}^2)^{3/2}$$

The alpha equation contains the error function:

$$\alpha(v_z) = K_c \operatorname{erf}(-4v_z/v_{th}) [\operatorname{erf}(-4(v_z - 19)/v_{th}) - \operatorname{erf}(4(v_z - 19)/v_{th})]$$

The substitution constant K_c was defined as:

$$K_c = v_{th}^2 \pi / 4 = [2kT/m] \pi / 4$$

The complication to this transformation was due to the eta function being dependent on v_x , v_y , and v_z . To provide an approximate dependence, I used the mean v_x value of v_{xo} to calculate the v needed for the eta function. The mean v_y value was zero, again neglecting the slight yaw. Mathematically, the correct equation for v changed from:

$$v = (v_x^2 + v_y^2 + v_z^2)^{1/2}$$

into:

$$v \approx (v_{xo}^2 + v_z^2)^{1/2}$$

Figure 3.14 plots a comparison of the results of the error function method versus the straight forward triple integral solution. The error function method overestimates the earlier result by roughly an order of magnitude at region 1 on the downwind side of the foil. The results compare closely on the upwind side of the foil, at region 5.

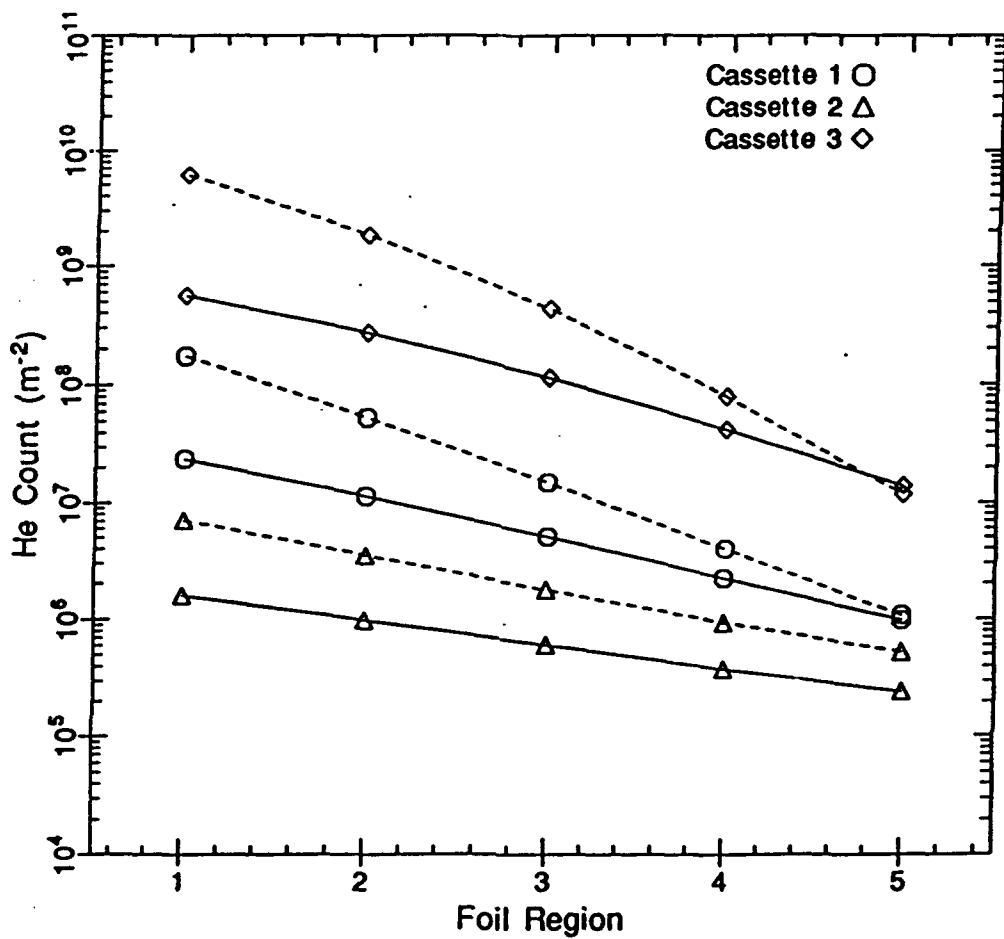


Fig. 3.14. A comparison of results for the number of helium particles per square meter of foil. The solid line represents the triple integral solution, the dashed line represents the error function solution.

The greatest advantage of this method is how rapidly it calculates out. The triple integration method of section 3.6.3 takes over 24 hours of processing time because of the repetitive numerical calculations at each increment of dv. The error function method effectively reduces the problem to a one-dimensional integration. Processing time is measured in seconds, not hours.

This chapter has outlined the development of several approaches to solving the problem, but how reliable are the results? The next chapter will look at inherent uncertainties in the calculations.

CHAPTER 4

RESULTS

Chapter 3 presented the development of the problem's solution. This chapter will examine possible sources of error in this solution. Different results would be expected if a different procedure had been used to provide the inputs for the MSIS model. Next, the integration would provide different results if the temperature and density inputs varied. This chapter will look at several questions. How does the MSIS model react to ranges in the input parameters? How responsive was the integration program to changes in temperature and density? How much uncertainty was introduced by the lack of low velocity data for the eta function? Finally, what can be done with these results, to enhance the IGE?

4.1 Variance of the Results

4.1.1 Varying the MSIS Input

The procedure I adopted chose one orbit at midmonth to represent the thermosphere for the entire month. The universal time, UT, input was always midnight. I checked how the output from MSIS changed by changing only the UT parameter for July 15, 1989. The orbit program ran six times for that day, beginning at midnight and stepping through the day, every four hours. The values for temperature and density were returned and averaged across the entire orbit. The mean MSIS results for temperature and helium density are plotted in figure 4.1.

Temperature ranged from 1140 to 1152, roughly one percent. Helium densities ranged from $2.8(10)^{12}$ to $3.7(10)^{12}$, roughly thirty percent. In this particular month the values chosen at midnight would underestimate the helium density and overestimate the temperature. This was due to the function's dependence on local solar time *and* the longitude input of RAAN. At other months the values chosen for midnight were representative of the midpoints of these ranges. There were also times when the UT input would underestimate the temperature and overestimate the density. The

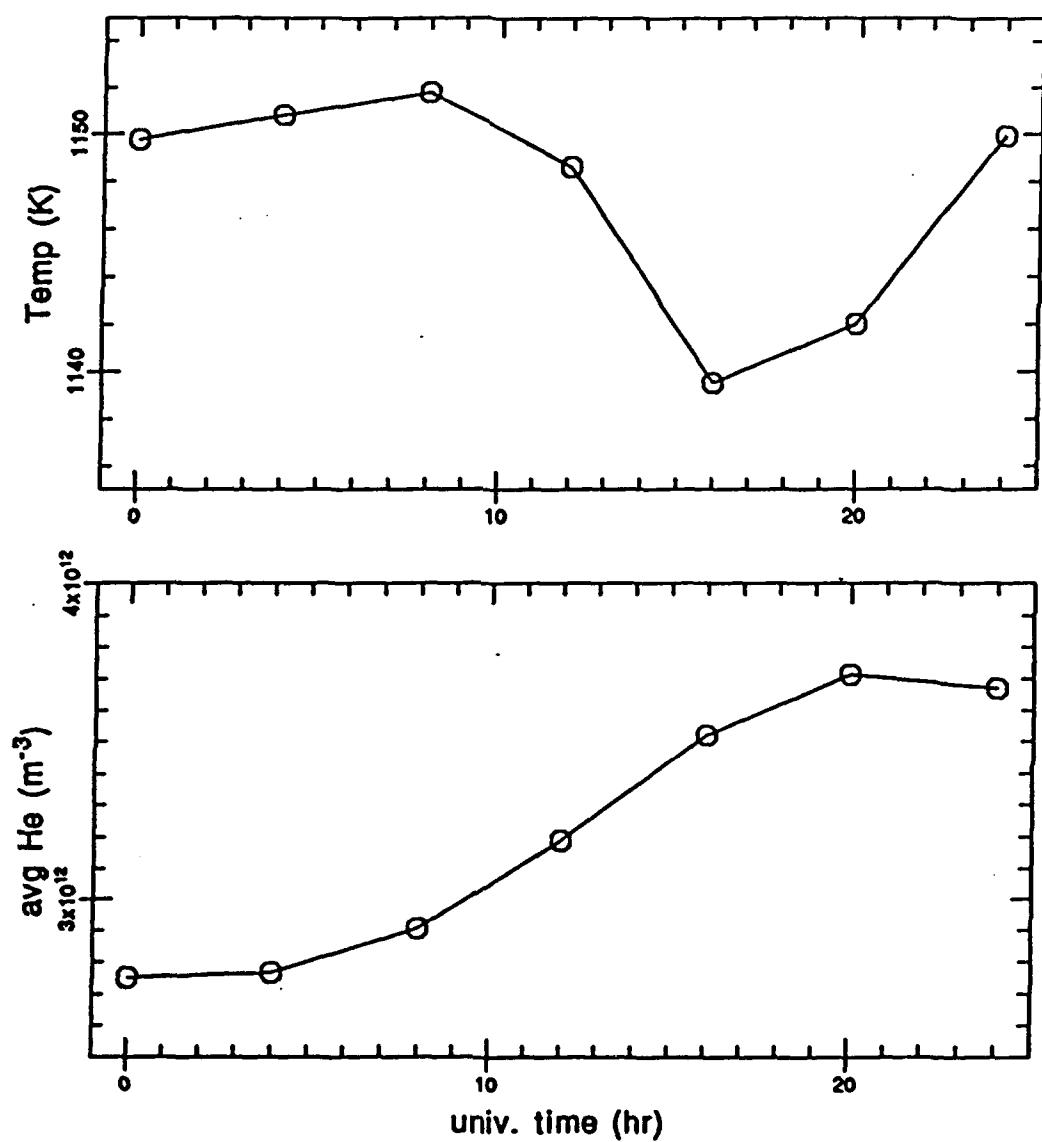


Fig. 4.1. The variance of MSIS computed temperature and helium density with universal time.

sampling of 140 of these calculations produced the overall mean of figure 3.4.

How did the data change across one month? For this experiment I altered the date by five day periods, beginning on the third of the month. UT was set at midnight; only the date input changed. The program averaged the data around one complete orbit for six months chosen at random. This data proved similar to the diurnal variation with the UT effect. Temperature ranges were less than one percent during solar quiet and helium densities varied as much as thirty percent. A review glance at figure 2.5 shows a rapid change in density from mid May to mid June, 1986. The rapid change was due to the equinox bulge when solar energy was concentrated at the equator. When the results were computed during a solar active month, temperature ranges increased. See figure 2.4. Note the 100 °C drop in temperature from mid June to mid July, 1989. This eight percent drop resulted from the erratic F10.7 indicator, which went from 247 in June to 188 in July, as shown in figure 2.1, for months 63 to 64. Density varied only four percent during this interval.

The next input varied was the right ascension at the ascending node, RAAN. The only input altered was this longitude, which was stepped eight times in 40° increments. The orbit code would use the longitude input with the universal time to determine the local solar time. The output would again be averaged across the entire orbit. This effect will depend on the diurnal cycle of the thermosphere. Figure 4.2 presents the results of this test, which was run on an equinox month, March, 1988, and a solstice month, December, 1988. The March data was nearly constant as the RAAN was altered. The December density ranged from $3(10)^{12}$ to $4(10)^{12}$, temperatures varied less than two percent.

4.1.2 Varying the Integration Input

The local solar time effect was very important. Figure 2.3 shows that helium density can change by a factor of three during one orbit. Temperature can vary by thirty percent. Since the Maxwell- Boltzmann velocity distribution function is exponential with a temperature dependance, small changes in temperature can be magnified by the distribution function.

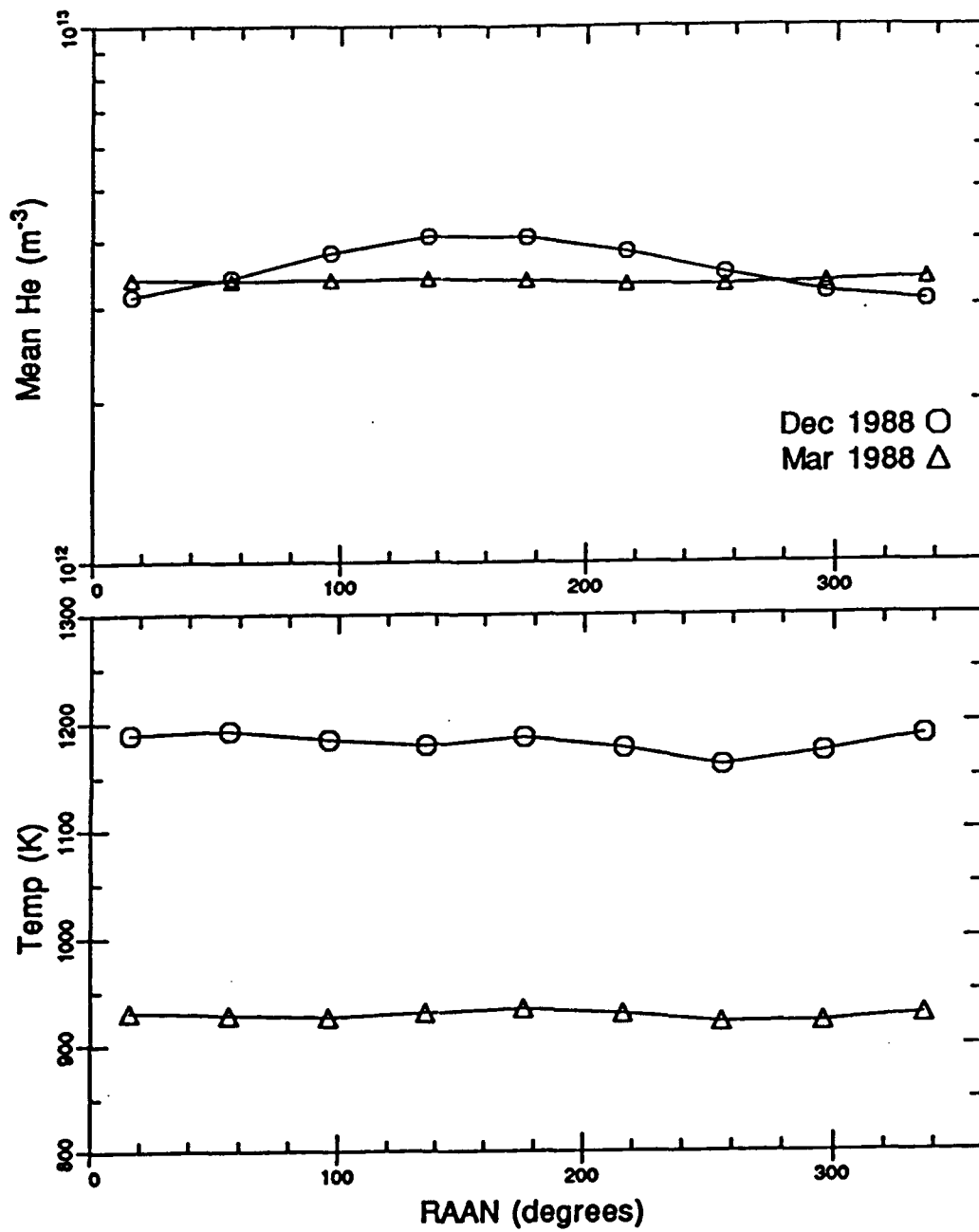


Fig. 4.2. The variance of MSIS computed temperature and helium density with the longitude of right ascension at the ascending node, RAAN.

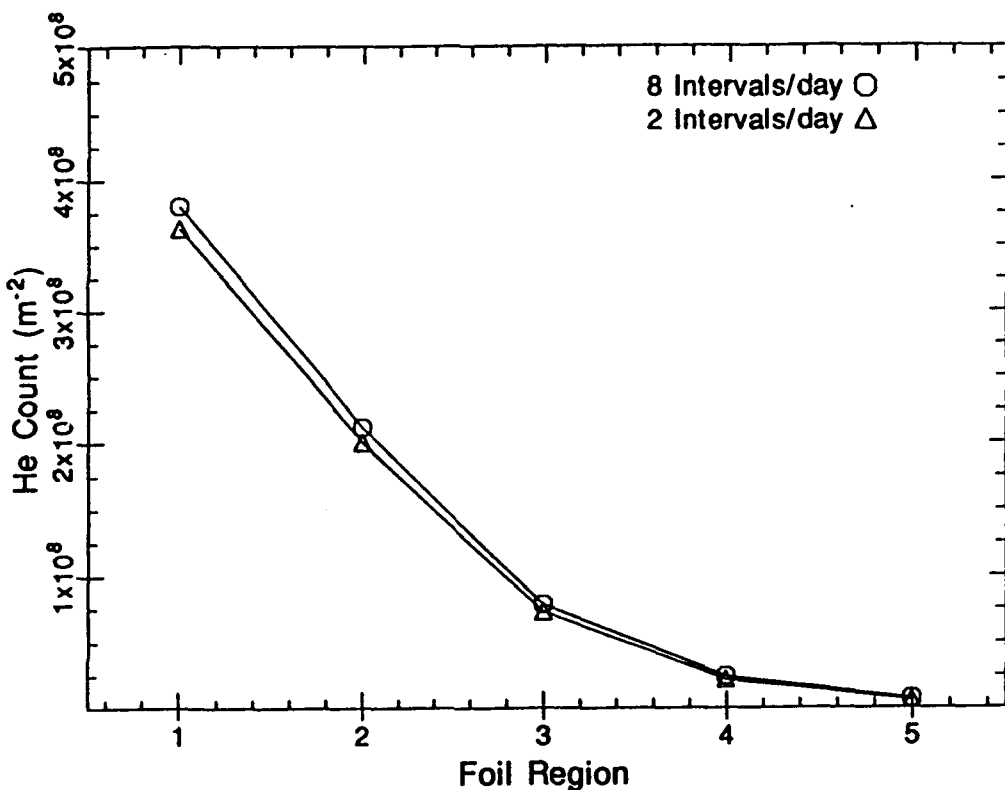


Fig. 4.3. A comparison of integration results for December, 1988, for foil cassette 3. The local solar time was segmented into eight three-hour bins, and two 12-hour bins, each with a mean temperature and density.

To explore the LST effect, for one month I averaged temperatures into eight three-hour bins. This data was then integrated to yield the helium count on the foil. The data from this trial was compared with the usual two 12-hour bins. Figure 4.3 displays the results. As expected, the eight hour integration results were slightly higher because of the higher temperature intervals. The downwind side of the foil, region 1, showed a five percent increase, the upwind side resulted in a no significant increase. This test was repeated for eight other months chosen randomly, all with similar results.

4.1.3 Varying the Eta Function

The largest source of uncertainty in the development of this solution resulted from the lack of low velocity data for the eta function. Figure 4.4 shows a representation of two Maxwellian velocity distribution functions. The top plot shows a distribution calculated with a temperature of 1400 °K. The lower plot was calculated with a temperature of 700 °K. The particle density decreases exponentially away from the origin. It drops off so rapidly that the probability of a particle having a velocity exceeding 20 km/s is essentially zero. Yet, it is only above 20 km/s where the eta function data has sufficient coverage to assure a high confidence fit. An experiment to determine the probability of adherence at low velocities would be very helpful.

To illustrate the range of uncertainty caused by the eta function, I developed a "low eta" and a "high eta" function. The overestimated eta was designed by fitting a line from the point defined by the two conditions, velocity equal to 20 km/s, eta equal to 10^{-5} , $(20, 10^{-5})$, to the point defined by velocity equal to zero and eta equal to zero, $(0, 0)$. The rest of the higher velocity probabilities were equal to the eta function described in section 3.5. Figure 4.5 plots this high eta function. The radical change of slope indicates that this should be a gross overestimate of the trapping probability. Similarly, the underestimated eta extended a line from the point, velocity equal to 25 km/s, eta equal to $4.6(10)^{-4}$ through the point $(20, 10^{-5})$. This line produced a zero probability of embedding into the foil at any velocity below 19.9 km/s. This value seemed too restrictive, indeed the integration proved to be zero particles for all foils. Another attempted fit chose the threshold value to be at the point, velocity equal to ten km/s, eta equal to zero. This low eta fit was equivalent to the best eta except for the threshold condition.

This low eta was then inserted into the integration program and executed. The results underestimated the original eta function by a factor of ten for the five foils aligned perpendicular to the virtual wind. When the high eta function was applied in the integration, the results overestimated the original eta function results by five orders of magnitude. These results are plotted in figure 4.6

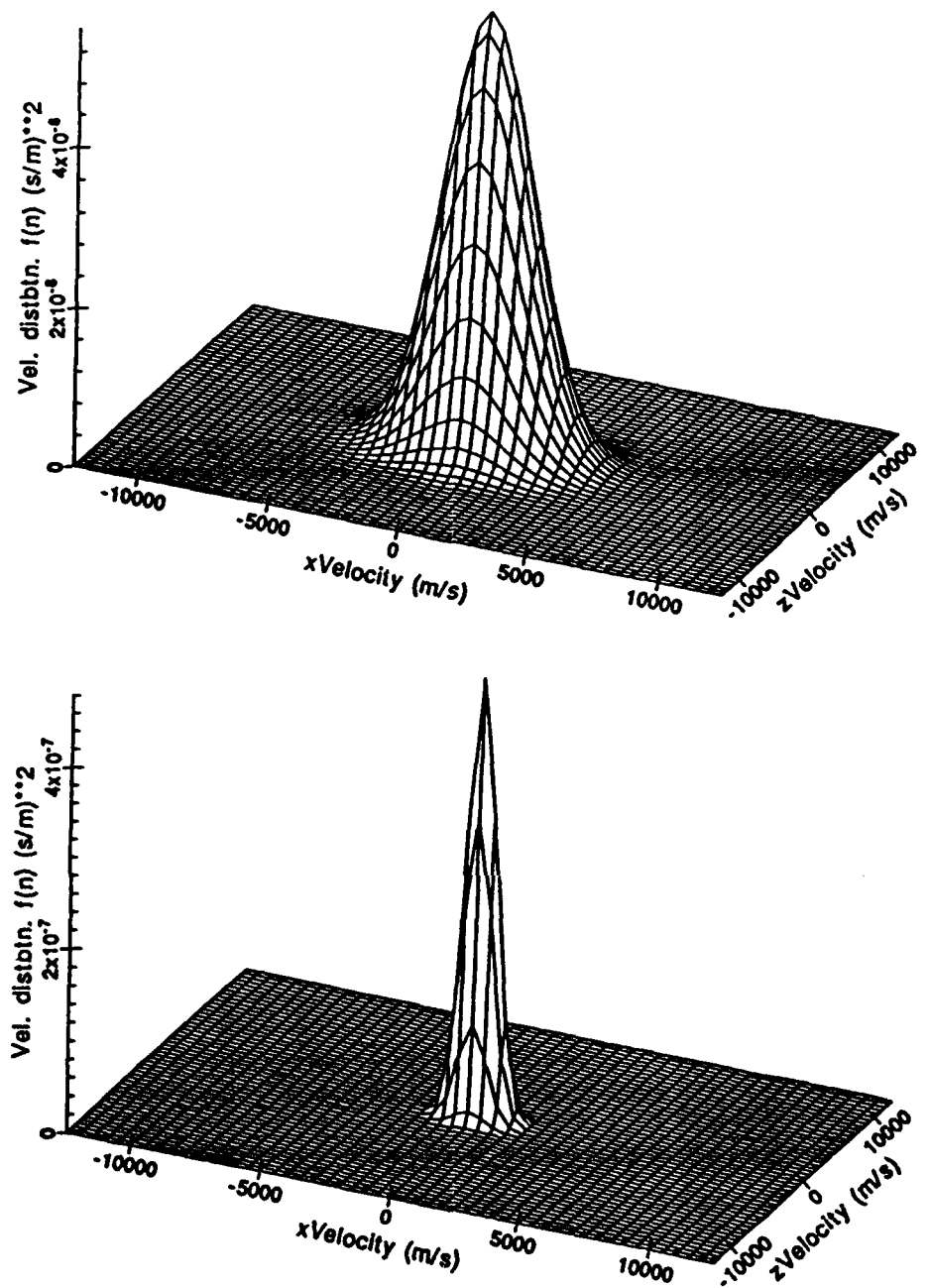


Fig. 4.4. Maxwellian velocity distributions for helium with zero bulk flow velocity and density of $3(10)^{12} \text{ m}^{-3}$. The top plot had a temperature of $1400 \text{ }^\circ\text{K}$; the bottom plot temperature was $700 \text{ }^\circ\text{K}$.

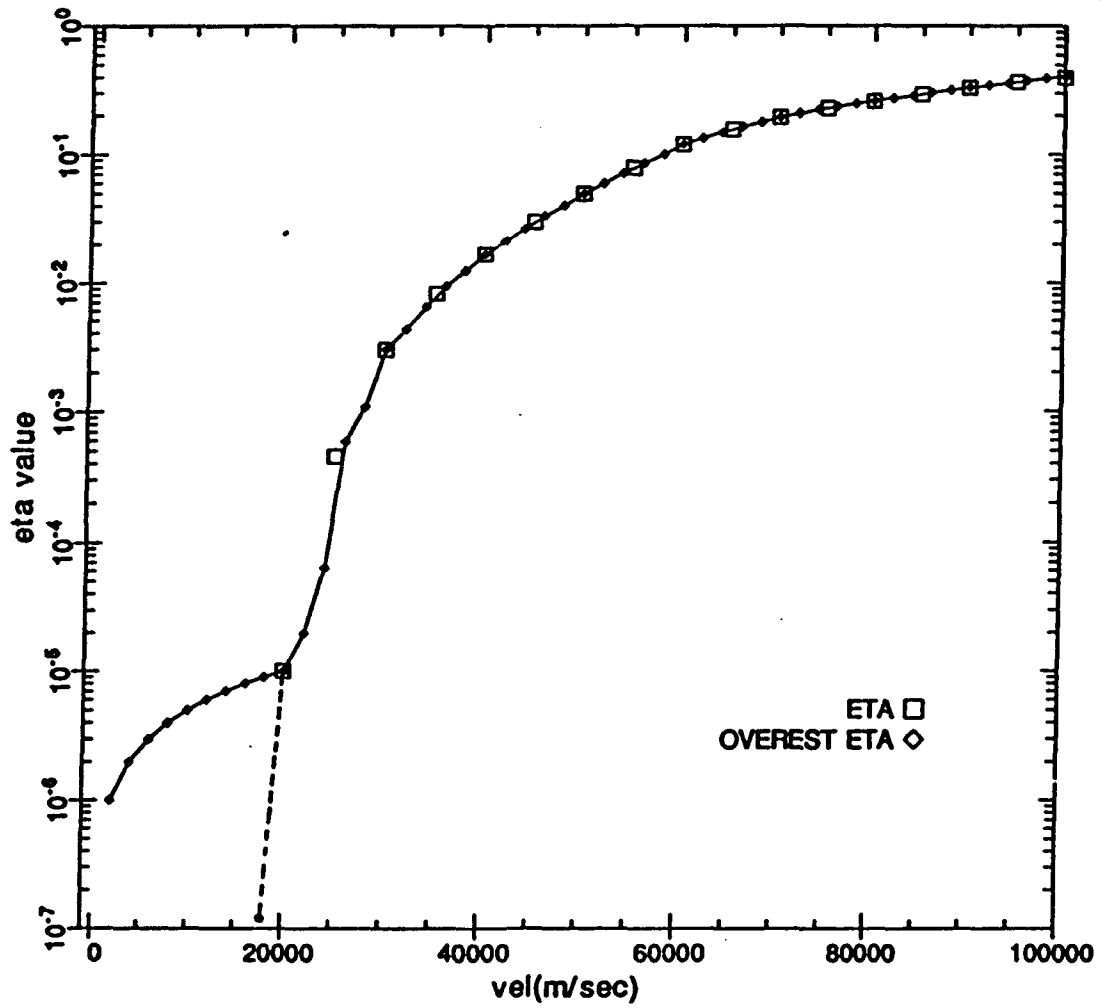


Fig. 4.5. A plot of an overestimate or high eta (solid line), and an underestimate, low eta, (dashed line) of the probability of a particle adhering to the foil.

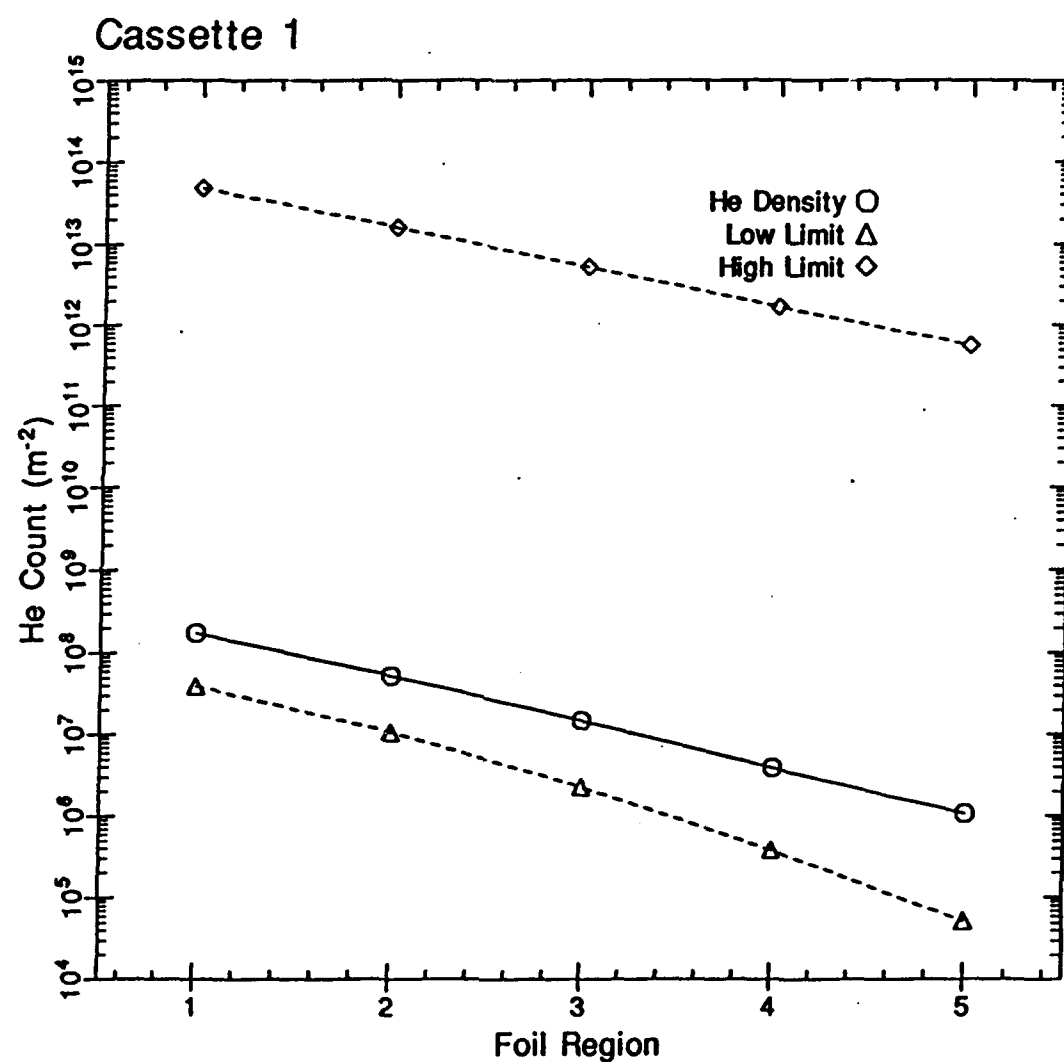


Fig. 4.6. The results for cassette 1 using the error function method. The dashed lines represent limits of uncertainty due to the eta function.

for all foils perpendicular to the velocity vector. Likewise figure 4.7 plots results for cassette 2, and figure 4.8 displays results for cassette 3.

The estimation of ^3He is based on the ratio of ^4He to ^3He . Latest research findings have this ratio at 1 to $1.42(10)^{-4}$ [Anders and Grevesse, 1989]. This ratio can be applied to the findings above to create a ^3He gradient as well.

4.2 Summary

The goal of estimating the number of atmospheric helium particles which accrued on each foil has been met. Beginning with the very wide range (0 to $(10)^{24}$), the range was brought into tighter focus. The fit of the eta function at low velocities limits the confidence of the final result, however, the midpoint of the foils should collect approximately $3(10)^7$ particles per square meter. Confidence estimates for the solution lying within the dashed line ranges of figure 4.6 through 4.8 were placed at 2/3. The answer could be lower if the threshold value for eta rose from ten km/s. Any uncertainties due to MSIS, or averaging methods, were dwarfed by this eta uncertainty.

Nevertheless, the terrestrial helium was considered background noise for the collection of interstellar helium. The collectors were designed to filter out the thermospheric helium. Figure 4.9 compares a few inherent differences between interstellar He and thermospheric He. These differences can be used to differentiate between the two, and isolate the interstellar He. The key result of this work is that the generous upper estimate of the background helium density is still low enough for the detection of interstellar gas particles.

The gradient across each foil has also been determined. The density gradient increases exponentially across the foil towards the downwind side. The uncertainty of the results decreases towards the upwind side of the foil because the higher velocity particles which impact region 5 depend on the better fitted domain of the eta function.

The gradients across each foil have a unique signature predicted by the model. Dr. J. Sojka noted that this trend should enable accurate subtraction of the background helium even if the absolute quantity is unknown.

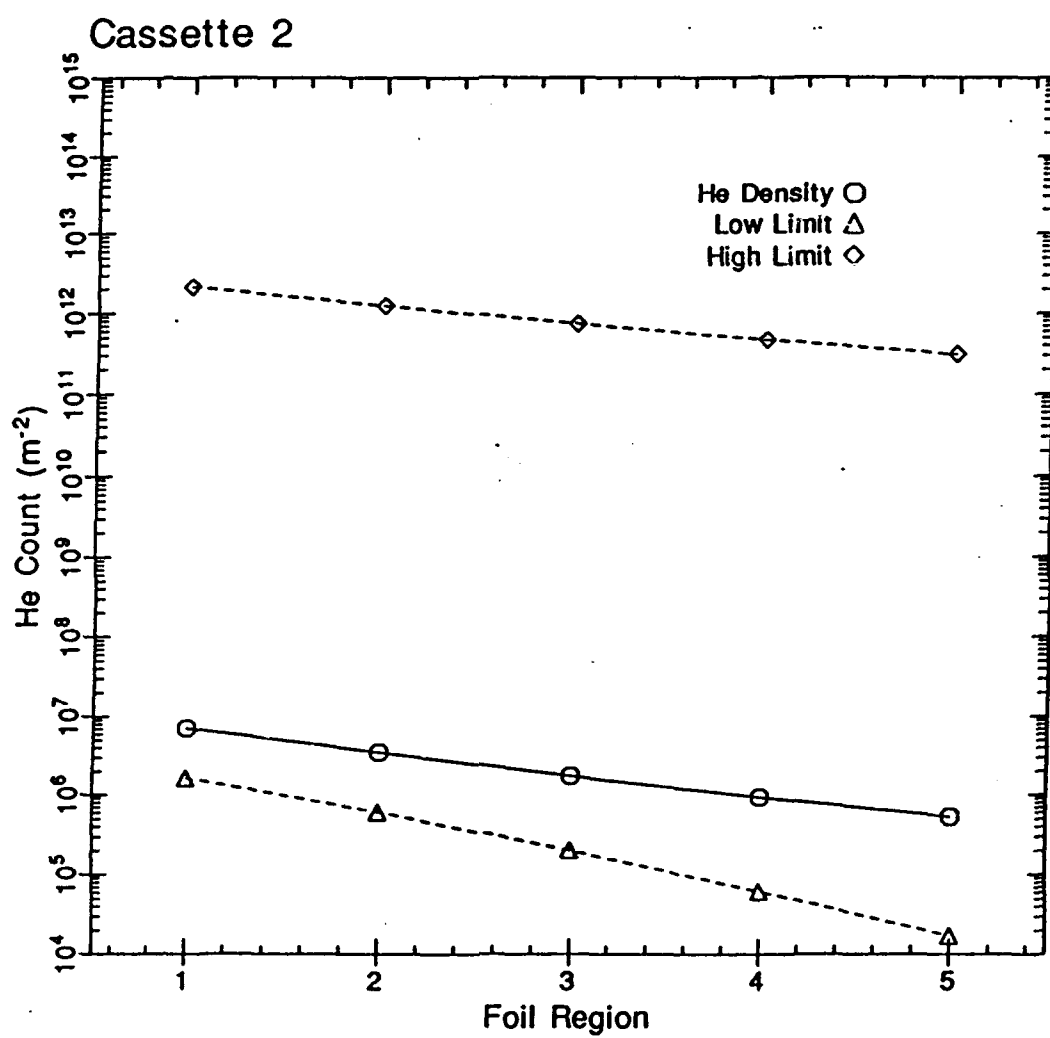


Fig. 4.7. The results for cassette 2 using the error function method. The dashed lines represent limits of uncertainty due to the eta function.

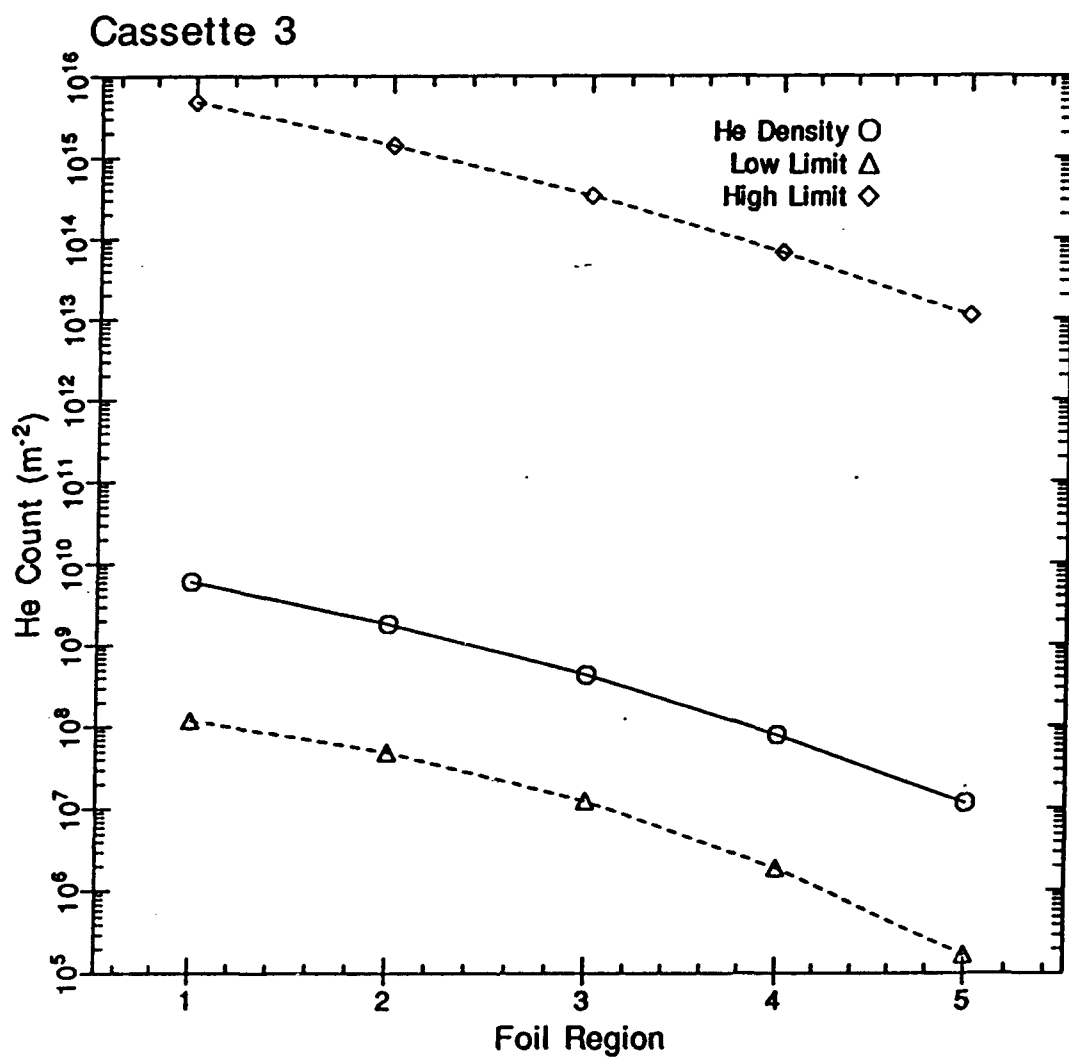


Fig. 4.8. The results for cassette 3 using the error function method. The dashed lines represent limits of uncertainty due to the eta function.

COMPARISON OF INTERSTELLAR He AND ATMOSPHERIC He

	INTERSTELLAR	ATMOSPHERIC
Velocity	24 km/s	0 km/s
Relative Velocity	24 km/s	7.6 km/s
Temperature	12000 °K	910 °K
Density	124 m^{-3}	$2.9(10)^{12} \text{ m}^{-3}$
Trapping Probability	$4(10)^{-4}$	$5(10)^{-13}$

Fig. 4.9. A comparison of parameters of interstellar helium and atmospheric helium.

4.3 Suggestions for Future Work

This calculation really needs a better set of data for the probability of a particle sticking to the foil at low velocities. If the data from such an experiment could hold uncertainties to less than a factor of two, the results from the flux calculation could be narrowed to plus or minus one order of magnitude.

One approach which might determine the trapping probability at low particle velocities was suggested by Dr. J. Sojka. Foil seven on tray E12 faced below the local horizon. The only helium particles which could have accrued on it were background from the thermosphere and particles precipitating along field lines from the magnetosphere. Since the model predicts a specific gradient, this would act as a fingerprint. The atmospheric helium actually found on this foil could be compared to the model's predicted values. Then the difference between these values can be used to determine a more accurate eta function.

The problem was well defined. The method for the calculation resulted from the specific geometry of the seven collectors. Each collector had its own field of view so the limits of integration were changed to model the specific view angles. The model was flexible enough to handle these changes.

This method can be applied to any passive collection system as long as it behaves as an ideal gas in thermal equilibrium. It could be applied to find the flux of any neutral species given by MSIS; for example, those shown in figure 2.10. To do this, the probability of the particles adhering to the foil data would have to be provided.

One aspect which could be looked at is, what if the particles were allowed one bounce prior to impacting the foil? This would take a new set of view angles into consideration, but the bulk of the calculation should remain the same. In this case, the foil's density distribution would show a second peak on the upwind side of the foil.

Another feature of this analysis is the difference in calculating time between the error function method and the straight ahead triple integral calculation. Depending on the accuracy required, a quick method for estimating any flux of this type would be to do two or three slow runs with the more accurate triple integration. Then do a few fast runs with the error function method. After comparison of the two results, create some fitting function which will transform the error function results to fit the triple integration results. The increase in processing time could be very practical, with less loss of accuracy than if the error function results were not modified.

The IGE mass spectrometer analysis is currently at a preliminary stage. The isotopes measured so far appear to be occurring at expected relative amounts. Two foils have been analyzed for an intensity gradient. A gradient has been found to exist and is in the correct direction [Lind *et al.*, 1991]. The gradients predicted by the model calculation are important. They will allow discrimination between atmospheric and interstellar helium. The critical isotope ratios can then be identified in the interstellar gas. These key ratios may reveal secrets of the early universe and of nucleosynthesis inside distant stars.

REFERENCES

- Anders, E., and Grevesse, N., Abundances of the elements: Meteoritic and solar, *Geochim. Cosmochim. Acta*, 53, 197, 1989.
- Fejer, B. G., Low latitude electrodynamic plasma drifts: A review, *J. Atmos. and Terr. Phys.*, 53, 677, 1991.
- Engebretson, M. J., and K. Mauersberger, The response of thermospheric atomic nitrogen to magnetic storms, *J. Geophys. Res.*, 88, 6331, 1983.
- Hedin, A. E., On MSIS, *personal correspondence*, May, 1991.
- Hedin, A. E., Extension of the MSIS thermospheric model into the middle and lower atmosphere, *J. Geophys. Res.*, 96, A2, 1159, 1991.
- Hedin, A. E., MSIS-86 thermospheric model, *J. Geophys. Res.*, 92, 4649, 1987.
- Hedin, A. E., N. W. Spencer, H. G. Mayr, and H. S. Porter, Semiempirical modeling of thermospheric magnetic storms, *J. Geophys. Res.*, 86, 3515, 1981.
- Hedin, A. E., J. E. Salah, J. V. Evans, C. A. Reber, G. P. Newton, N. W. Spencer, D. C. Kayser, D. Alcayde, P. Bauer, L. Cogger, and J. P. McClure, A global thermospheric model based on mass spectrometer and incoherent scatter data MSIS 1. N₂ density and temperature, *J. Geophys. Res.*, 82, 2139, 1977.
- Hedin, A. E., H. G. Mayr, C. A. Reber, N.W. Spencer, and G. R. Carignan, Empirical model of thermospheric temperature and composition based on data from the Ogo-6 quadrupole mass spectrometer, *J. Geophys. Res.*, 79, 215, 1974.
- Herrero, F. A., and J. W. Meriwether Jr., 6300-A Airglow meridional intensity gradients, *J. Geophys. Res.*, 85, 4191, 1980.
- Killeen, T. L., and R. G. Roble, Thermospheric dynamics: Contributions from the first five years of the Dynamics Explorer program, *Reviews of Geophysics*, 26, 329, 1988.
- Knecht, D. J., and B.M. Shuman, The Geomagnetic Field, *Handbook of Geophysics and the Space Environment*, Jursa, A. S., ed., 4-1, 1985.
- Lind, D.L., J. Geiss, F. Buhler, and O. Eugster, The Interstellar Gas Experiment, *NASA correspondence*, Aug, 1991.
- Lind, D.L., J. Geiss, P. Eberhardt, A. J. Steed, and F. J. Redd, The Interstellar Gas Experiment - 2 Proposal, *NASA AO OSSA 2-88*, Sep, 1988.
- Mayr, H. G., and H. Volland, Magnetic storm effects in the neutral composition, *Planet. Space Sci.*, 20, 379, 1970.

- McPherson, P. H., and H. Rishbeth, Thermospheric temperatures over Malvern: a comparison of incoherent scatter data with two global thermospheric models, *J. Atmos. and Terr. Phys.*, 41, 1021, 1979.
- Prolss, G. W., Perturbation of the low-latitude upper atmosphere during magnetic substorm activity, *J. Geophys. Res.*, 87, 5260, 1982.
- Sojka, J. J., Global scale, physical models of the F region ionosphere, *Reviews of Geophysics*, 27, 371, 1989.
- Thompson, D.C., and W.J. Raitt, A numerical model of the interaction of contaminant neutral gases released from orbiting spacecraft with ambient terrestrial atmosphere, Ph.D dissertation, 118 pp., Utah State University, Logan, UT, 1989.